

https://dspace.org/

Machine learned CalabiYau metrics and curvature

Per Berglund; Giogri Butbaia; Tristan Hubsch; Vishnumohan Jejjala; Damian M Pena ...

INT PRESS BOSTON, INC
https://hdl.handle.net/10539/44660
WOS

Downloaded from a DSpace repository. https://dspace.org/

ADV. THEOR. MATH. PHYS.
Volume 27, Number 4, 1107–1158, 2023

Machine learned Calabi–Yau metrics and curvature

Per Berglund, Giorgi Butbaia, Tristan Hübsch, Vishnu Jejjala, Damián Mayorga Peña, Challenger Mishra, and Justin Tan

Finding Ricci-flat (Calabi–Yau) metrics is a long standing problem in geometry with deep implications for string theory and phenomenology. A new attack on this problem uses neural networks to engineer approximations to the Calabi–Yau metric within a given Kähler class. In this paper we investigate numerical Ricci-flat metrics over smooth and singular K3 surfaces and Calabi–Yau threefolds. Using these Ricci-flat metric approximations for the Cefalú family of quartic twofolds and the Dwork family of quintic threefolds, we study characteristic forms on these geometries. We observe that the numerical stability of the numerically computed topological characteristic is heavily influenced by the choice of the neural network model, in particular, we briefly discuss a different neural network model, namely spectral networks, which correctly approximate the topological characteristic of a Calabi–Yau. Using persistent homology, we show that high curvature regions of the manifolds form clusters near the singular points. For our neural network approximations, we observe a Bogomolov–Yau type inequality $3c_2 \geq c_1^2$ and observe an identity when our geometries have isolated A_1 type singularities. We sketch a proof that $\chi(X \smallsetminus \operatorname{Sing} X) + 2\,|\operatorname{Sing} X| = 24$ also holds for our numerical approximations.

1 Introduction, rationale, and summary **1108**

2 The testbed models and their curvature **1109**

3 Numerical methods **1119**

4 Results **1122**

5 Conclusions **1147**

Appendix A Numerical integration **1150**

Appendix B Plurisubharmonic property (metric positivity) **1151**

Appendix C Classical volume terms dominate **1151**

References **1153**

1. Introduction, rationale, and summary

Ricci-flat metrics satisfy the Einstein equations without any energy-momentum tensor source, and so describe empty spacetime. They are thus of fundamental physical interest and have been studied intensely for over a century. The closely related Kähler metrics on compact, complex geometries of Euclidean signature — the Calabi–Yau spaces — describe (to lowest order) the extra spacelike dimensions in string compactifications.

While many Calabi–Yau properties are accessed purely via topology, knowledge of the Ricci-flat metric is crucial for certain explicit computations, such as finding α' corrections, fixing the Kähler potential, determining Yukawa couplings, and deducing aspects of supersymmetry breaking in the low-energy effective field theory [1–3]. All of these are prerequisites for calculating the proverbial electron mass in a Standard Model derived from string compactification.

Yau's proof [4, 5] of the Calabi conjecture [6] is famously not constructive. We know that a Calabi–Yau manifold has a unique Ricci-flat metric in each Kähler class, but not the actual expressions for such metrics. In recent years, there has been revived interest in obtaining Ricci-flat Calabi–Yau metrics. On the analytical side, explicit expressions have been obtained for the metric on certain K3 manifolds [7, 8].[1] On the computational side, various machine learning techniques have been employed to obtain numerical as well as spectral approximations to flat metrics [10–18]. In some of these machine driven approaches, neural networks have provided new representations to study metrics over manifolds with special holonomy. Although there are guarantees to a neural network's ability to approximate reasonably well behaved functions with arbitrary accuracies, there are further mathematical

[1]The analytic expression for the flat metric on the Calabi–Yau onefold was written by Clifford in 1873 [9].

guarantees for neurocomputing stemming from the powerful Kolmogorov–Arnold representation theorem from the middle of the previous century. To date, the state of the art in approximating Ricci-flat Calabi–Yau metrics using machine learning methods is the `cymetric` code [14, 19], which permits us to obtain approximate flat metrics for complete intersection (CICYs), as well as toric Calabi–Yau spaces derived from triangulations of reflexive polytopes from the Kreuzer–Skarke list [20]. Past efforts to obtain flat metrics include the so-called Donaldson's algorithm [21–23] as well as applications of the Gauss–Seidel method in [24], the optimization of energy functionals [25], and examination of scaling properties [26, 27]. (See also [28–32].)

In this paper, we apply machine learning techniques to singular and non-singular K3 manifolds and quintic threefolds. One of the goals of this work is to characterize how good the machine learned metrics are for phenomenology. In order to perform this assessment, we consider computations of topological quantities such as the Euler character and the Chern classes as obtained from the metric — as well as the corresponding curvature *distributions*. Thereby, we seek to determine which parts of the geometry contribute most significantly to the various topological quantities. To benchmark these observations, it is useful to compare the Fubini–Study metric to the machine learned metric.

We also propose a different neural network model, called *spectral networks*, for approximating the Ricci-flat metric. We find that the numerical invariants computed using the spectral networks exhibit higher numerical stability than standard fully-connected networks which directly use the homogeneous coordinates as input. Furthermore, we briefly discuss the final loss achieved by these networks and find that for Fermat quartic, the lowest σ-loss is below 10^{-3}, which is at the same level of accuracy as the method described in [25] using $k = 8$.

The organization of this paper is as follows. Section 2 describes the deformation families of Calabi–Yau twofolds and threefolds we investigate in this paper and the considered curvature related features. Section 3 briefly summarizes the numerical methods we apply. Section 4 considers the machine learned metrics. Certain details of numerical computations are discussed in the appendices.

2. The testbed models and their curvature

We consider several simple, one parameter deformation families of Calabi–Yau twofolds and threefolds. In each case, we focus on a few curvature related

features for which we compare the results obtained with a numerical approximation to the Ricci-flat metric, with those obtained using the pullback of the Fubini–Study metric, as well as with the known exact results.

2.1. The deformation families

The Cefalú pencil: Consider a complex one parameter deformation family of quartics in $\mathbb{P}^3$ [33]:

$$\mathbb{P}^3 \supset X_\lambda := \{p_\lambda(z) = 0\} : \quad p_\lambda(z) := \sum_{i=0}^{3} z_i^4 - \frac{\lambda}{3}\left(\sum_{i=0}^{3} z_i^2\right)^2 . \tag{1}$$

The Cefalú hypersurface [33] is the $\lambda = 1$ case. We call the general λ deformation, the Cefalú family (pencil) of quartics. While this deformation family of hypersurfaces provides for a rather more detailed analytic analysis [34–37], we focus on a few immediate results for the purpose of comparing with numerical computations of the metric and various metric characteristics on these K3 surfaces. For each $\lambda \in \mathbb{C}$, the defining polynomial $p_\lambda(z)$ is manifestly invariant under all permutations of the z_i, as well as sign changes $z_i \mapsto -z_i$, separately for each $i = 0, 1, 2, 3$. Subject to preserving the holomorphic two-form, $\Omega := \oint \frac{(z\, \mathrm{d}^3 z)}{p_\lambda(z)}$, *viz.*, the Calabi–Yau condition, and modulo the $\mathbb{P}^3$-projectivization, this generates an $S_4 \times (\mathbb{Z}_2)^2$ symmetry. Of the various possible quotients, here we only need $X_0/\mathbb{Z}_2$. The overall situation is sketched in Figure 1, and includes both the λ-plane of the hypersurfaces (1) as well as the λ-plane of their $\mathbb{Z}_2$ quotients.

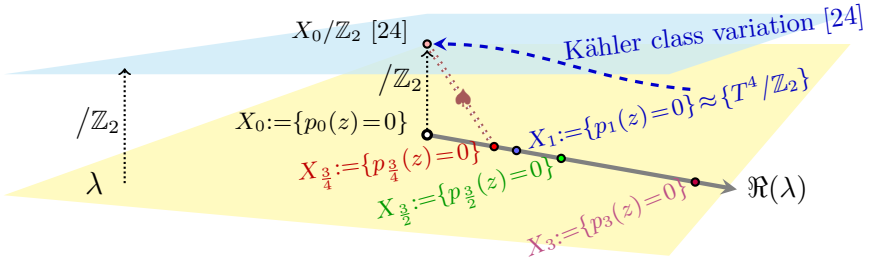

Figure 1. The Cefalú (complex structure) deformation family of quartics (1) (lower λ-plane), and their $\mathbb{Z}_2$ quotients (upper plane), together with the identifications $X_1 \approx \{T^4/\mathbb{Z}_2\}$ and $X_{\frac{3}{4}} \approx \big(X_0/\mathbb{Z}_2\big)$, the latter identification labeled by "♠".

Variation of λ parametrizes a deformation of the complex structure of the hypersurface X_λ, while the subsequently discussed numerical computation of the various metric characteristics is explicitly designed, as in (35), to preserve the Kähler class of the embedding $\mathbb{P}^3$. The defining polynomial $p_\lambda(z)$ fails to be transverse only for $\lambda \to \lambda^\sharp \in \{\frac{3}{4}, 1, \frac{3}{2}, 3\}$ in the finite[2] λ-plane ($|\lambda| < \infty$), and the quartic hypersurface, X_λ, singularizes there and has, respectively: 8, 16, 12, and 4 isolated singular points. Each of these singular points is an A_1-singularity (*i.e.*, *node* or *double point*): the gradient of the defining equation (1) vanishes there, but the Hessian (matrix of second derivatives in local coordinates) is regular; for any other *A-D-E* (so-called Du Val) singular point the local Hessian would vanish.[3] The singularities of each $X_{\lambda^\sharp}$ are thus all hypersurface singular points of the form $(0,0,0) \in \{xy = z^2\} \subset \mathbb{C}^3$ in local coordinates, and are also equivalently described as discrete quotient (orbifold) singularities of the form $(0,0) \in \mathbb{C}^2/\mathbb{Z}_2$. Deforming any of the singular hypersurfaces $X_{\lambda^\sharp} \to X_{\lambda^\sharp + \epsilon}$ for $|\epsilon| \ll 1$ changes its complex structure and smooths it by replacing each of its nodes with an S^2-like so-called *vanishing cycle* of radius $\propto |\epsilon|$.

Alternatively and without changing either λ or the complex structure in general, each node can also be desingularized by a blow-up. This surgically replaces each node with a copy of the (again S^2-like) so-called *exceptional set*, which admits a compatible complex structure and is biholomorphic[4] to the *complex* projective space, $\mathbb{P}^1$ — and changes the overall Kähler class by contributing[5] a (variable) multiple of the Kähler class inherent to the

[2] At $\lambda \to \infty$, the vanishing of $p_\infty = \big(\sum_i {z_i}^2\big)^2$ defines an "*everywhere singular*" hypersurface (more properly, a *scheme*), X_∞, since $\vec{\partial} p_\infty(z)$ vanishes wherever $p_\infty(z)$ does. Also, denoting $Z_\infty := \{\sum_i {z_i}^2 = 0\}$, we have that $X_\infty = Z_\infty \cup Z_\infty$ is an everywhere doubled space, which is singular at $X^\sharp_\infty = Z_\infty \cap Z_\infty$ — indeed, everywhere. In this respect, the $\lim_{\lambda\to\infty} X_\lambda$ limit is an extremely degenerate case of Tyurin degenerations [38].

[3] All the relevant details and facts about these singularities and their (complex structure variation) deformations and (Kähler class variation) desingularizations are found in Reid's comprehensive survey [39].

[4] In fact, it is the total space of the $\mathcal{O}_{\mathbb{P}^1}(-2)$ line bundle over this $\mathbb{P}^1$ that replaces the excised singularity compatibly with the global complex structure of the quartic hypersurface. The tangent bundle being $T_{\mathbb{P}^1} = \mathcal{O}_{\mathbb{P}^1}(2)$, the adjunction theorem implies that the patching preserves c_1. Also, the self-intersection of this exceptional $\mathbb{P}^1$ is then -2.

[5] In the overall Kähler metric, $g^{(0)}_{ab}$, defined without/before the blow-up, the exceptional set replacing a point is *null*; $g^{(0)}_{ab}$ continues to "see" it as a point. To correct this, one varies the metric by adding a local contribution inherent to the exceptional set.

exceptional $\mathbb{P}^1$. Such Kähler class variations were studied in [24] and were shown by numerical computation to connect the orbifolds $T^4/\mathbb{Z}_2$ and $X_0/\mathbb{Z}_2$. By desingularizing $T^4/\mathbb{Z}_2$ via blowup and successively increasing the size of the exceptional sets, these eventually intersect and form new $\mathbb{Z}_2$-orbifold singularities, the so-obtained singular space identifiable with $X_0/\mathbb{Z}_2$.

Explicit λ-deformation connects $X_1 \to X_{\frac{3}{4}}$ by varying the complex structure while holding the Kähler class constant. One would expect the vanishing cycles of $X_{1-\epsilon}$ to grow as $\epsilon \in [0, \frac{1}{4})$, come closer to each other and intersect as $\epsilon \to \frac{1}{4}$, creating the singularities of $X_{\frac{3}{4}}$. On the other hand, the number, type and highly symmetric distribution of singularities in the hypersurfaces $X_{\frac{3}{4}}$ and X_1 suggests identifying these with the two global orbifolds considered in [24], resulting in an interesting double connection (the "$\approx$" symbols denote a likely but not rigorously proven identification):

$$\{X_0/\mathbb{Z}_2\} \approx X_{\frac{3}{4}} \xrightarrow[\text{cpx. str. deform}]{\lambda} X_1 \approx \{T^4/\mathbb{Z}_2\}\,. \tag{2}$$

Kähler class variation [24]

For the *crepant* (c_1-preserving [40]) desingularization of both of these orbifolds, the Euler characteristic may be computed by

$$\chi\big(\widetilde{M/G}\big) = \frac{1}{|G|}\big(\chi(M) - \chi(F)\big) + \chi(N)\,, \tag{3}$$

where M is a smooth manifold with the discrete group action G for which F is the fixed point set and N the desingularizing surgical replacement of F; for a complete and detailed refinement see [41] and [40, § 4.5]. Assuming a similar identification with a global finite quotient to be possible also for $X_{\frac{3}{2}}$ (and X_3), since these have 12 (4) isolated A_1-singular points, both with $|G = \mathbb{Z}_2| = 2$ and where N consists of 12 (4) isolated exceptional $\mathbb{P}^1$s with $\chi(\mathbb{P}^1) = 2$, we compute

$$\frac{1}{2}\big(\chi(M_{\frac{3}{2}}) - 12\big) + 12{\cdot}2 = 24 = \chi(\widetilde{X_{\frac{3}{2}}}) \quad\Longrightarrow\quad \chi(M_{\frac{3}{2}}) = 12\,; \tag{4a}$$

$$\frac{1}{2}\big(\chi(M_3) - 4\big) + 4{\cdot}2 = 24 = \chi(\widetilde{X_3}) \quad\Longrightarrow\quad \chi(M_3) = 36\,. \tag{4b}$$

Here, $M_{\frac{3}{2}}$ (M_3) denotes a nonsingular complex surface with a $\mathbb{Z}_2$ action that has 12 (4) fixed points, the $\mathbb{Z}_2$-orbifolds of which may be identified with $X_{\frac{3}{2}}$ (X_3). Whereas in (2), we have $M_{\frac{3}{4}} \approx X_0$ (the Fermat quartic) and $M_1 \approx T^4$, we do not have any obvious candidate for $M_{\frac{3}{2}}$ and M_3, but note that these would have to have $h^{2,0} \geqslant 1$, and that precisely one holomorphic

volume form must remain after the $\mathbb{Z}_2$ quotient. Since $X_{\frac{3}{4}+\epsilon}$, $X_{1+\epsilon}$, $X_{\frac{3}{2}+\epsilon}$ and $X_{3+\epsilon}$ are all smoothed by a "$\lambda^\sharp \to \lambda^\sharp + \epsilon$" (complex structure) deformation, they are conceptual mirrors of the (Kähler class variation) desingularizations indicated in (3) and (4).

The Dwork pencils: Analogous to the Dwork pencil of quintics [34]

$$\mathbb{P}^4 \supset Z_\psi := \big\{Q_\psi(z) = 0\big\} : \quad Q_\psi(z) := \sum_{i=0}^{4} {z_i}^5 - 5\psi \prod_{i=0}^{4} z_i \,, \tag{5}$$

we also consider the Dwork pencil of quartics

$$\mathbb{P}^3 \supset Y_\psi := \big\{q_\psi(z) = 0\big\} : \quad q_\psi(z) := \sum_{i=0}^{3} {z_i}^4 - 4\psi \prod_{i=0}^{3} z_i \,. \tag{6}$$

Following the by now well known analysis of the quintic (5), it is easy to show that $\psi \simeq \alpha\psi$, with $\alpha^4 = 1$, so $\mathrm{Arg}(\psi) \in [0, \pi/2]$ provides a fundamental domain, subject to identifying the edges $\{\mathrm{Arg}(\psi) = 0\} \simeq \{\mathrm{Arg}(\psi) = \pi/2\}$, thus forming a cone. The two families (1) and (6) are related: evidently, $Y_0 = X_0$. Furthermore, $q_\psi(z)$ fails to be transverse only for $\psi = \alpha$ with $\alpha^4 = 1$, where Y_α has 16 isolated A_1-singular points, $(1, \alpha\beta^{2i}\gamma^{3j}, \alpha\beta^i\gamma^{2j}, \alpha\beta^i\gamma^{3j})$ for $\alpha^4 = \beta^4 = \gamma^4 = 1$ and $i, j = 0, \ldots, 3$. Thus, Y_1 has the same number and type of isolated singular points as X_1 (albeit in different locations), and as in Figure 1, we identify $Y_1 \approx X_1 \approx \{T^4/\mathbb{Z}_2\}$. This implies that within the K3 complex structure moduli space, the λ-plane and the ψ-cone have two points in common: $(\lambda = 0) = (\psi = 0)$ and $(\lambda = 1) = (\psi = 1)$. Finally, we note that the Y_∞ model is a complex projective *tetrahedron*, the union of four $\mathbb{P}^2$s that meet in six $\mathbb{P}^1$s that meet in four points. Unlike X_∞ (which is singular everywhere), Y_∞ is singular only at the union of those six $\mathbb{P}^1$s.

2.2. General remarks on Kähler geometry

Since it is a complex, Kähler manifold, the Calabi–Yau metric is Hermitian and can be obtained from a Kähler potential $K(z, \bar{z})$:

$$g_{a\bar{b}} = \partial_a \partial_{\bar{b}} K(z, \bar{z}) \,. \tag{7}$$

The corresponding Kähler form, written in terms of the metric, reads

$$J = \frac{\mathrm{i}}{2} g_{a\bar{b}}\, dz^a \wedge d\bar{z}^{\bar{b}} \,. \tag{8}$$

As a consequence of Kählerity, the only non-zero Christoffel symbols are those for which holomorphic and antiholomorphic indices do not mix:

$$\Gamma^a_{bc} = \overline{\Gamma^{\bar{a}}_{\bar{b}\bar{c}}} = (\partial_b g_{c\bar{d}}) g^{\bar{d}a} \,. \tag{9}$$

From this, we readily compute the non-zero components of the Riemann tensor:

$$R^a_{b\bar{c}d} = -\bar{\partial}_{\bar{c}} \Gamma^a_{bd} \,, \quad R^a_{\bar{b}cd} = \bar{\partial}_{\bar{b}} \Gamma^a_{cd} \,, \tag{10}$$

together with

$$R^a_{b\bar{c}d} = \overline{R^{\bar{a}}_{\bar{b}c\bar{d}}} \,, \quad R^a_{\bar{b}cd} = \overline{R^{\bar{a}}_{b\bar{c}\bar{d}}} . \tag{11}$$

The only non-vanishing entries for the Ricci tensor of a Kähler metric are given by

$$R_{a\bar{b}} = R^c_{ca\bar{b}} = -\partial_a \partial_{\bar{b}} \log \det g \,. \tag{12}$$

We may sometimes write $\det g = |g|$. R is closed but not necessarily exact. It serves to define the Ricci form $\mathrm{Ric}(J) = \mathrm{i} R_{a\bar{b}} dz^a \wedge d\bar{z}^{\bar{b}}$ which is closed by construction. Since $c_1(J)$ is required by the Calabi–Yau condition to be zero, the Ricci form of a Calabi–Yau is also exact. For further details, the reader should consult the classic references [40, 42, 43].

The Riemann tensor can be used to construct the curvature form

$$\mathcal{R}^a_b = R^a_{bm\bar{n}} dz^m \wedge d\bar{z}^{\bar{n}} \,. \tag{13}$$

We then have

$$\mathrm{Tr}\, \mathcal{R} \;\; = R^a_{am\bar{n}} dz^m \wedge d\bar{z}^{\bar{n}} = -\mathrm{i}\, \mathrm{Ric}(J) \,, \tag{14}$$

$$\mathrm{Tr}\, \mathcal{R}^2 = R^a_{bm_1\bar{n}_1} R^b_{am_2\bar{n}_2} dz^{m_1} \wedge d\bar{z}^{\bar{n}_1} \wedge dz^{m_2} \wedge d\bar{z}^{\bar{n}_2} \,, \tag{15}$$

$$\mathrm{Tr}\, \mathcal{R}^3 = R^a_{bm_1\bar{n}_1} R^b_{cm_2\bar{n}_2} R^c_{am_3\bar{n}_3} dz^{m_1} \wedge d\bar{z}^{\bar{n}_1} \wedge dz^{m_2} \wedge d\bar{z}^{\bar{n}_2} \wedge dz^{m_3} \wedge d\bar{z}^{\bar{n}_3} \,, \tag{16}$$

which can be used to obtain the various Chern characteristic forms $c_i \in \Omega^{i,i}(\mathcal{M})$, resulting from the expansion

$$c(t) = \det\left(1 + \frac{\mathrm{i}t}{2\pi} J\right) = c_0 + c_1 t + c_2 t^2 + \dots \,. \tag{17}$$

Written in terms of the curvature form, the corresponding Chern forms are given by

$$c_0 = 1\,, \tag{18}$$

$$c_1 = \frac{\mathrm{i}}{2\pi}\mathrm{Tr}\,\mathcal{R}\,, \tag{19}$$

$$c_2 = \frac{1}{2(2\pi)^2}(\mathrm{Tr}\,\mathcal{R}^2 - (\mathrm{Tr}\,\mathcal{R})^2)\,, \tag{20}$$

$$c_3 = \frac{1}{3}c_1\wedge c_2 + \frac{1}{3(2\pi)^2}c_1\wedge \mathrm{Tr}\,\mathcal{R}^2 - \frac{\mathrm{i}}{3(2\pi)^3}\mathrm{Tr}\,\mathcal{R}^3\,. \tag{21}$$

For complex n-dimensional manifolds, X, $\int_X c_n$ is the Euler characteristic so the top Chern class, c_n, is also the Euler (curvature) density $e(J) = c_n(J)$. For $\dim(X) = 2$ CY, c_2 may be further identified with the standard volume form multiple of the Kretschmann invariant of Ricci-flat metric, the tensor norm-square of the Riemann tensor; see (22), below. As an additional check on Ricci-flatness, this approximation has been studied in [24].

Restricting to the Calabi–Yau twofold and threefold examples of relevance to this paper, we have that the Euler densities simplify for the Ricci-flat metric due to the condition $c_1 = 0$. For K3 we expect the Euler density to be

$$c_2(J^{\mathsf{CY}}) = \frac{1}{2(2\pi)^2}\mathrm{Tr}\,\mathcal{R}^2 = \frac{1}{8\pi^2}\sqrt{g}\; R_{a\bar{b}c\bar{d}}\,R^{a\bar{b}c\bar{d}}\;\mathrm{d}^4z\,, \tag{22}$$

and similarly for a Calabi–Yau threefold

$$c_3(J^{\mathsf{CY}}) = -\frac{\mathrm{i}}{3(2\pi)^3}\mathrm{Tr}\,\mathcal{R}^3\,. \tag{23}$$

Note however that the above expressions only hold for the Ricci-flat Calabi–Yau metric. Since we only have numerical approximations to this and since we're interested in checking how well-defined is the resulting metric approximated using neural networks (See Section 4.3), our curvature density estimates are always obtained by means of (20) and (21).

2.3. Topological checks and the curvature distribution

In the pursuit of computing the Ricci-flat metric by varying an initial choice such as the Fubini–Study metric on the embedding projective space, it behooves to verify that computationally feasible and otherwise known quantities, such as the Euler number, continue to be evaluated accurately.

For complex surfaces, the second Chern class is the Euler density, which is given by the following:

$$\begin{aligned}\chi_{\text{E}} &= \int_{\text{K3}} c_2 = \frac{1}{2(2\pi)^2}\int_{\text{K3}} (\operatorname{Tr}\mathcal{R}^2 - (\operatorname{Tr}\mathcal{R})^2)\\ &= \int_{\text{K3}} \mathrm{d}^4z\,\sqrt{g}\rho - \frac{1}{2(2\pi)^2}\int_{\text{K3}} (\operatorname{Tr}\mathcal{R})^2\,,\end{aligned} \tag{24}$$

where ρ is the Kretschmann scalar, which may be more familiar from general relativity, where it is used to distinguish coordinate singularities from physical singularities, and is analogous to the $F_{\mu\nu}F^{\mu\nu}$ term in gauge theory. In nearly singular hypersurfaces $X_{\lambda^\sharp+\epsilon}$, the Euler density receives significant contributions from the vicinity of the vanishing cycles, these being heavily curved and nearly singular. For small enough but nonzero ϵ, these regions are also well separated since they limit to isolated singular points in the $\epsilon\to 0$ limit, and it is possible to exclude the contribution from these large curvature regions.

The numerically computed Euler density distribution indeed turns out to be heavily peaked near zero, indicating that a relatively large portion of the hypersurface harbors little curvature. The distribution however also has a long and thin "tail," indicating rather small (rarely sampled) but highly curved regions. The bulk of the contributions sampled at essentially randomly distributed points therefore misses these "curvature peaks." For example, in the actually singular hypersurfaces at the special choices $\lambda=\lambda^\sharp$, the Euler number computation using the Fubini–Study metric finds:

1) At $\lambda=\frac{3}{4}$, $\chi(X_{\frac{3}{4}})_{\mathsf{FS}}\approx 8$, missing the contribution of 8 singular points;
2) At $\lambda=1$, $\chi(X_1)_{\mathsf{FS}}\approx -8$, missing the contribution of 16 singular points;
3) At $\lambda=\frac{3}{2}$, $\chi(X_{\frac{3}{2}})_{\mathsf{FS}}\approx 0$, missing the contribution of 12 singular points;
4) At $\lambda=3$, $\chi(X_{\frac{3}{4}})_{\mathsf{FS}}\approx 16$, missing the contribution of 4 singular points.

This is consistent with the fact that all singular points are A_1-singularities, the blow-up of each of which contributes $\chi(\mathbb{P}^1)=2$, completing the result to $\chi(X_\lambda)=24$ (the "stringy," *i.e.*, *equivariant* Euler number [41]) even for these singular quartics.

The numerical computation of the Euler density and its integral (the Euler number) to a predetermined precision shows that a significantly larger number of sampling points is required for the nearly singular X_λ than for X_λ with λ far from the four special values, $\lambda^\sharp$.

2.4. Some useful results for (singular) K3s

The singular K3 manifolds considered in this work are $\mathbb{P}^3_{\mathbb{C}}$ embedded projective surfaces with isolated singularities. Since the singularities prevent definition of smooth forms (such as curvature form J on X), we may consider the smooth locus $X_s \subseteq X$ and induce a curvature form J using the pullback of Fubini–Study metric on $\mathbb{P}^3_{\mathbb{C}}$. This action, however bears the cost of $c_n \in \Omega^{n,n}(X_s)$ no longer carrying the topological information of X. In order to study the topological Euler characteristic of the resulting variety, we instead consider Chern–Schwartz–MacPherson classes $c_{\rm SM}$ [44–46]. In particular, we have the following relation between the $c_{\rm SM}(X)$ and the topological Euler characteristic $\chi(X)$ of a possibly singular variety X [47]:

$$\chi(X) = \deg c_{\rm SM}(X)\,. \tag{25}$$

Furthermore, we may relate the Fulton class $c_F(X)$ to the Chern–Schwartz–MacPherson characteristic class $c_{\rm SM}(X)$ using [48, 49]:

$$(-1)^{\dim X} \deg(c_F(X) - c_{\rm SM}(X)) = \sum_{p\in \text{Sing } X} \mu_X(p)\,, \tag{26}$$

where $\mu_X(p)$ is the Milnor number of the singularity $p \in \text{Sing } X$. The actual Euler number can be computed with aid of Proposition 1, which we prove.

Proposition 1. *Let $X \subseteq \mathbb{P}^3_{\mathbb{C}}$ be a possibly singular projective surface with curvature form J defined on the smooth locus X_s of X. If $|\text{Sing } X| < \infty$ and the singularities are of type A_1, then:*

$$\int_{X_s} e(J) + 2|\text{Sing } X| = \deg c_F(X)\,, \tag{27}$$

where $c_F(X)$ is the Fulton class of X and $e(J)$ is given by Pfaffian: $\text{Pf}(J)/(2\pi)^2$.

Proof. Build a stratification of X in the following manner: define

$$X_0 := X \setminus \text{Sing } X = X_s$$

and for every singular point $p_i \in \text{Sing } X$, define $X_i := \{p_i\}$. Note that X_0 is the largest stratum, and X_i for $i > 0$ are the singular strata. Using the results from [50], we may express the integral of Pfaffian $\text{Pf}(J)$ on X_s in terms of the local Euler obstructions $\text{Eu}_p(X)$ [44] as:

$$\frac{1}{4\pi^2}\int_{X_s} \text{Pf}(J) = \chi(X) - \chi(\text{Sing X}) + \sum_{p\in \text{Sing} X} \text{Eu}_p(X)\,\chi(\{p\})\,, \tag{28}$$

where we have $\chi(X_s) = \chi(X) - \chi(\text{Sing } X)$ since X is a complex projective variety and $|\text{Sing } X| < \infty$. Furthermore, $\chi(\text{Sing } X) = |\text{Sing } X|$. Thus, the proof reduces to computation of $\chi(X)$ and the Euler obstructions $\text{Eu}_p(X)$ for $p \in \text{Sing } X$. Using the results of [51], we may express $\text{Eu}_p(X)$ in terms of the Milnor numbers:

$$\text{Eu}_p(X) = 1 - (-1)^{\dim X}\mu_{X\cap H}(p)\,, \tag{29}$$

where H is a generic hyperplane through $p \in \text{Sing } X$. In case of $\dim_{\mathbb{C}} X = 2$, for A_1 type singularities $p \in \text{Sing } X$, we have $\mu_{X\cap H}(p) = 1$ (see [52, 53]), thus, the Euler obstructions vanish. Using the identity (26) and the property of Chern–Schwartz–MacPherson classes (25), we have:

$$\begin{aligned}\chi(X) = \deg c_{\text{SM}}(X) &= \deg c_F(X) - \sum_{p\in \text{Sing } X} \mu_X(p)\\ &= \deg c_F(X) - |\text{Sing } X|\,.\end{aligned} \tag{30}$$

Thus, by combining the results, we obtain:

$$\frac{1}{4\pi^2}\int_{X_s} \text{Pf}(J) = \deg c_F(X) - 2|\text{Sing } X|\,, \tag{31}$$

which concludes the proof. □

It is easy to see that the singularities of singular X_λ varieties in the Cefalú pencil ($\lambda < \infty$) are of type ${A_1}^6$. Furthermore, we may regard the

[6]By symmetry of the defining polynomial, all singularities have equal Milnor number; moreover, it equals 1, in agreement with the analysis in Section 2.1.

Cefalú pencil as a smoothing family near each singular $X_{\lambda'}$. Using [50], we have the following identity:

$$\lim_{\lambda\to\lambda'}\lim_{\delta\to 0}\int_{X_\lambda\cap N_\epsilon(\text{Sing } X)} e(J_\lambda) = (-1)^2\left[\sum_{p\in\text{Sing } X}\mu_X(p)+\mu_{X\cap H}(p)\right] = 2|\text{Sing } X|\,. \tag{32}$$

From [54–57] it is known that for surfaces admitting Kähler–Einstein metric with curvature form J, the characteristic forms $c_2(J)$ and $c_1(J)$ satisfy the Bogomolov–Yau (BY) inequality:

$$3c_2(J) - c_1(J)^2 \geq 0\,. \tag{33}$$

3. Numerical methods

3.1. Calabi–Yau metrics from neural networks

Here we briefly review the existing paradigm of approaches based on direct prediction of the metric tensor by a neural network [10–14]. Focusing, for example, on the Calabi–Yau threefold case, the metric tensor in local coordinates has a representation as a Hermitian 3×3 matrix, with three independent off-diagonal complex parameters and three independent diagonal real parameters. The first order approach would be to have the neural network predict nine real components in local coordinate charts such that the metric tensor satisfies the Ricci-flatness conditions on the Calabi–Yau geometry. However, this may be overly general, and we can consider more restrictive ansätze (classes of functions which the neural network may represent) that may help the approximation.

By Yau's theorem [5], any compact Kähler manifold of complex dimension n with vanishing first Chern class admits a unique Ricci-flat metric in each of its $h^{1,1}$ Kähler classes. That is to say, given a choice of reference metric g_{ref} with Kähler form J^{ref} on the Calabi–Yau X, there exists a Kähler form J^{CY} associated with the unique Ricci-flat metric. J^{CY} is cohomologous to J^{ref} and hence given by an exact correction:

$$J^{\mathsf{CY}} = J^{\mathsf{ref}} + \mathrm{i}\partial\bar\partial\phi\,. \tag{34}$$

Here, $\phi\in C^\infty(X)$ is a global smooth real function on X. If X is embedded into a projective space (or a product of projective spaces), the reference

Kähler form on X may be taken to be the pullback of the canonical Fubini–Study form in the ambient space, J^{FS}. To approximate the true Ricci-flat metric on X, one may estimate the correction term in (34) by employing a neural network to model $\phi_{\mathsf{NN}} : X \to \mathbb{R}$ via a patch invariant scalar function using local coordinate points, and then subsequently pulling back to X.

Assuming one has found an embedding of the Calabi–Yau X in the ambient space, $\iota : X \hookrightarrow \mathcal{A}$, the Ansatz for the predicted metric g_{CY} takes the following form:[7]

$$g_{\mathsf{CY}} \triangleq \iota^* g_{\mathsf{FS}} + \partial\bar{\partial}\phi_{\mathsf{NN}} \,. \tag{35}$$

By computing the eigenvalue distribution (see Appendix B), we verify that the so-defined metric, g_{CY}, continues to be positive (Riemannian), but defer the analysis[8] of the necessary and sufficient conditions for that throughout the computational framework. While positivity is not explicitly enforced, the metric is symmetric by construction and its determinant is encouraged to be positive by the objective function. If ϕ is a global function, the associated Kähler form is remains in the same Kähler class as J^{ref}. However, if ϕ changes between coordinate patches, then this is not guaranteed, and further precautions must be taken to preserve the Kähler class.

To compute the approximations of the Calabi–Yau metric for twofolds, we use the `cymetric` library [14, 19]. For Calabi–Yau threefolds, we also use a custom implementation of the routines in the `cymetric` library in `JAX` [58], with extended functionality for computing topological quantities. The `cymetric` package supports different approaches to numerically approximating the Ricci-flat metric. The model (35) is known as the `PhiModel`. We use the `PhiModel` to obtain metric approximations for the K3 and quintic examples and the `JAX` implementation for the quintic examples only. For the underlying neural network model which approximates ϕ, we use a fully connected/dense network with 3 hidden layers and 64 nodes in each hidden layer; see Figure 2.[9]

A variation of this algorithm is to make ϕ_{NN} invariant under $\mathbb{C}^*$ from the beginning. Instead of taking real and imaginary parts of the homogeneous coordinates as inputs, one can take the following: $z_i\bar{z}_i/|z|^2$, $\mathrm{Re}(z_i\bar{z}_j/|z|^2)$, $\mathrm{Im}(z_i\bar{z}_i/|z|^2)$ ($j < i$, where $i, j = 1, ..., N+1$). Thus, instead of $2(N+1)$ we have $(N+1)^2$ inputs for this modified neural network. This results in a

[7] With a slight abuse of notation, (35) should be interpreted component-wise.

[8] We thank Oisin Kim for constructive discussion on this subtlety.

[9] We train for 50 epochs, with batch sizes: $(64, 50000)$ using Adam optimizer with the default parameters. We use gelu activation functions.

globally defined function ϕ_{NN} on $\mathbb{P}^N_{\mathbb{C}}$. We briefly describe the results derived from this method in Section 4.3, and leave a more detailed survey of these techniques for an upcoming publication [59].

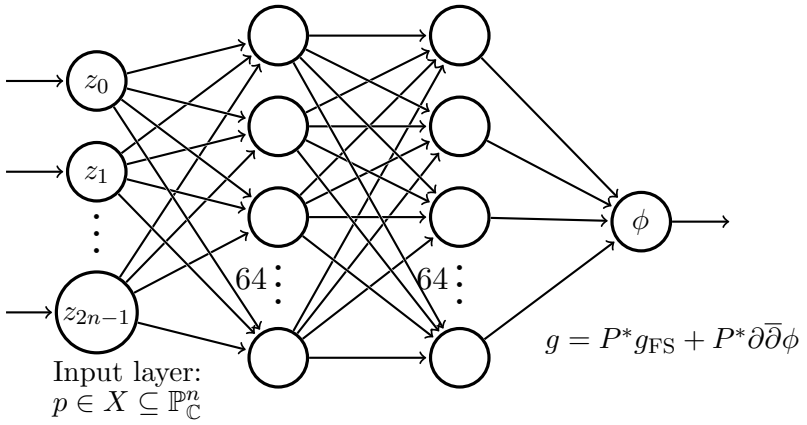

Figure 2. Neural-network architecture for building the `PhiModel` using `cymetric`.

3.2. Persistent homology

Let $f : \Sigma \to \mathbb{R}$ be a function on a simplicial complex Σ such that whenever σ_1 is a facet of σ_2 in Σ, $f(\sigma_1) \leq f(\sigma_2)$. For $x \in \mathbb{R}$, define the level set $\Sigma_x = f^{-1}(I_x)$, with $I_x = (-\infty, x]$; this is a subcomplex of Σ. The ordering of values of f on the simplices in Σ defines a filtration,

$$\emptyset = \Sigma_0 \subseteq \Sigma_1 \subseteq \ldots \subseteq \Sigma_n = \Sigma\,. \tag{36}$$

For $p \leq q$, we have the k-th persistent homology group $H_k^{p,q}(\Sigma)$ that is induced by the inclusion $\Sigma_p \hookrightarrow \Sigma_q$. In particular, we have homomorphisms $f_k^{p,q} : C_k(\Sigma_p) \to C_k(\Sigma_q)$ modulo boundaries, with $C_k(\Sigma_p)$ the free Abelian group generated by k-simplices in Σ_p. The *persistent homology groups* are the images of these homomorphisms, and the Betti numbers $b_k^{p,q}$ are the dimensions of these groups. Proceeding across the filtration, topological features are born and die. For instance, connected components may be added to the space, cycles can form or be filled in, etc. The *barcode* is a graphical way of visualizing this information. Persistent homology provides a microscope that images the shape of a dataset and is a key tool in topological data analysis. We use this to identify high curvature regions on Calabi–Yau spaces.

4. Results

In our analysis we compute the various curvature forms using both the pullback of the Fubini–Study metric from the ambient space (FS) and the machine learned approximation to the Ricci-flat metric (ML). This approach has various advantages. First, having the explicit expressions for the Chern forms in the case of the Fubini–Study metric, we can ensure that the numerical errors in the topological computations are solely due to the Monte Carlo (MC) integration. The Fubini–Study metric then serves to check convergence of the integration as we increase the number of points. This also provides a consistency check for the computations leading to the Euler number in the various examples considered. These results clarify which limitations are due to the numerical integration and which limitations are due to the machine learned approximation. As an *hors d'œuvre* we present the

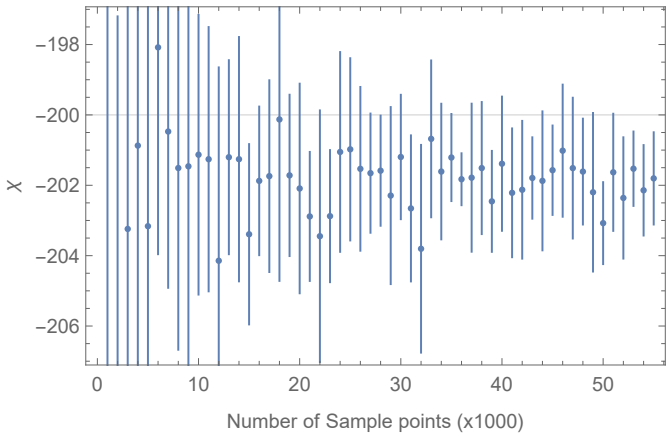

Figure 3. Euler number for the Fermat quintic $Y_{\psi=0}$ computed using different numbers of sample points.

convergence results for the Monte Carlo integration for the Euler density of the Fubini–Study metric. Consider the Fermat quintic $Y_{\psi=0}$ and take a dataset of $100,000$ points uniformly distributed with respect to the pullback Fubini–Study metric. Then we take a subsample of a given size, ranging from $1,000$ to $55,000$, and for each subsample size we repeat the experiment ten times. For a given subsample, we compute the Euler density and out of the ten repetitions we obtain an estimate of the error (by means of the standard deviation). The results are shown in Figure 3.

We observe that the variance reduces as the number of points is increased. For $100,000$ points we obtain an Euler number of $\chi = -196.43$,

roughly 2% off the expected value. In the simplest compactifications of the heterotic string, the number of generations of particles in the low energy spectrum is given by the index of the Dirac operator and is $\frac{1}{2}|\chi|$. Being off by even 1% for the quintic reports the wrong number of families of elementary particles (in the standard embedding of Heterotic String compactifications).

4.1. Characteristic forms on the Cefalú pencil

Let J_λ be a curvature form on X_λ. In the case of singular X_λ, (24) is no longer true. In studies of moduli dependent metrics [11, 24], it has been observed that the accuracy of the approximately flat metric is moduli dependent. These ideas prompt us to analyze the performance of neural network based approaches for studying Calabi–Yau spaces which are singular or nearly singular. In particular, we numerically compute the integral (24) using the curvature forms J_λ^{FS} and J_λ^{CY} calculated using the induced and numerical Calabi–Yau metrics, respectively. The numerical values of the Euler characteristic for different X_λ in the vicinity of singular $X_{\lambda^\sharp}$ are shown in Figure 4. Using the fully-connected network approximation of ϕ, we observe a decreasing trend of the accuracy as we approach the singular $X_{\lambda^\sharp}$ varieties in the pencil. In particular, we note that the Euler characteristic computed using the machine learned approximation to the Calabi–Yau metric deviates significantly from the expected value of 24 by a margin that is too large to be attributed to the numerical Monte Carlo integration. Furthermore, we see a significant discrepancy between the numerical values computed using J_λ^{FS} and J_λ^{CY} at the singular X_λ. From Figure 4, we notice that for the cases $\lambda = 1$ and $\lambda = 3$ we obtain the most significant discrepancies between Fubini–Study and machine learned results.

In order to make sense of the results for singular X_λ's, let us consider the degrees of the Chern–Schwartz–MacPherson classes which are presented in Table 1 and the Monte Carlo computations for the Fubini–Study metric shown in Table 2. To compute the $c_{\mathrm{SM}}(X_\lambda)$ and $c_F(X_\lambda)$ we use Macaulay2 [60]. From these tables we can see that the numerical results are in agreement with Proposition 1.

We also notice that the Fubini–Study results satisfy the Bogolomov–Yau inequality (33). Note, however, that for singular X_λ, we have a non-zero value for the numerical approximation of the integral of the first Chern class. That is,

$$\int_{X_{\lambda^\sharp} \setminus \mathrm{Sing}\ X_{\lambda^\sharp}} c_1(J_\lambda^{\mathsf{FS}})^2 \neq 0\,, \tag{37}$$

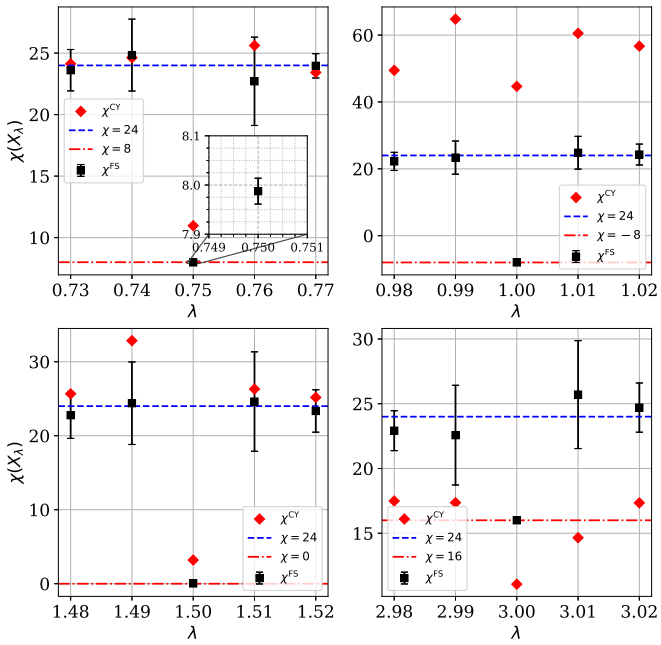

Figure 4. Numerical values of (24) along the Cefalú pencil. Black points and error bars showing a 95% confidence interval are associated to Fubini–Study results, while the red dots correspond to the machine learned metric approximation using fully-connected networks. See the Appendix for details on integration.

λ	$\deg c_{\mathrm{SM}}(X_\lambda)$	$\deg c_F(X_\lambda)$	$\lvert\mathrm{Sing}\ X_\lambda\rvert$
0	24	24	0
3/4	16	24	8
1	8	24	16
3/2	12	24	12
3	20	24	4

Table 1. Degrees of Fulton and Chern–Schwartz–MacPherson classes for Cefalú pencil.

λ	# of sing. pt.	$\deg c_2(J_\lambda^{\mathsf{FS}})$	$\deg c_1(J_\lambda^{\mathsf{FS}})^2$	$\deg(3c_2(J_\lambda^{\mathsf{FS}}) - c_1(J_\lambda^{\mathsf{FS}})^2) \geq 0$
0	0	24	0	True
3/4	8	7.99 ± 0.03	-16.0 ± 0.2	True
1	16	-7.99 ± 0.08	-31.9 ± 0.3	True
3/2	12	0.0 ± 0.1	-23.9 ± 0.3	True
3	4	16.00 ± 0.09	-8.0 ± 0.1	True

Table 2. Values of the integrals of the possible top characteristic forms on X_λ. The integrals were evaluated using MC integration. The uncertainties correspond to 95% confidence interval.

as shown in Table 2. In addition, note that Table 2 exhibits the following property:

$$\int_{X_{\lambda^\sharp} \smallsetminus \text{Sing } X_{\lambda^\sharp}} c_2(J) - c_1(J)^2 = 24 = \chi(\text{K3})\,, \tag{38}$$

which prompts us to formulate the following conjecture.

Conjecture 1. *Let $X \subseteq \mathbb{P}^3_{\mathbb{C}}$ be a possibly singular K3 surface, whose smooth locus X_s has curvature form J induced by the Fubini–Study metric on $\mathbb{P}^3_{\mathbb{C}}$. If the singularities of X are isolated and of type A_1, then* (38) *holds true.*

For a singular algebraic surface $X_{\lambda^\sharp}$ with $\lambda^\sharp < \infty$, the crepant (c_1-preserving) desingularization of an isolated A_1-singularity replaces it with an exceptional $\mathbb{P}^1$-like divisor, S, with the self-intersection $[S]^2 = -2$.

The $\deg c_1(J_\lambda^{\mathsf{FS}})^2$ column in Table 2 evidently equals the total sum of these isolated contributions — as if $X_{\lambda^\sharp}$ was desingularized. We thus arrive at the next conjecture.

Conjecture 2. *Each $X_{\lambda^\sharp}$ in* (1) *with $\lambda^\sharp < \infty$ may be identified with a global finite quotient, and the* $\deg c_2(J_\lambda^{\mathsf{FS}})$ *column contributions to $\chi(K3)$ in Table 2 appropriately display the leading term in* (3).

This corroborates our expectation that $X_{3/2}$ and X_3 are also identifiable as global finite $\mathbb{Z}_2$ quotients as shown in (4).

We note that Conjecture 1 fails if the singular locus of X contains a singularity of dimension greater than zero, which is possible for geometries that combine the Dwork and the Cefalú deformations.

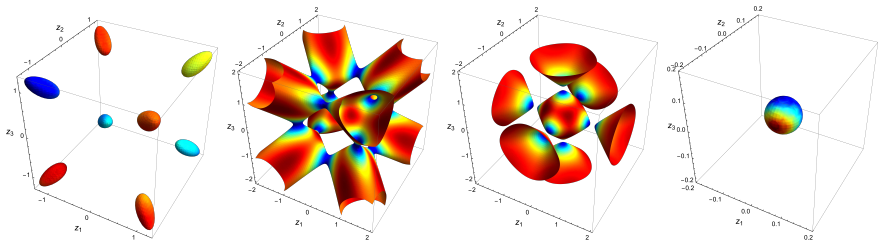

(a) $\lambda = 0.77$ (b) $\lambda = 1.01$ (c) $\lambda = 1.51$ (d) $\lambda = 2.98$

Figure 5. Visualization of the real subset of $X_{\lambda^\sharp+\epsilon}$ in a patch $\{z_0 \neq 0\}$. The coloring is defined by the values of the trained spectral network ϕ. (See Section 4.3.)

We shall separately consider each singular $X_{\lambda^\sharp}$ in the following. The visualizations of ϕ for some near-singular surfaces X_λ are shown on Figure 5. The training progress is shown on the Figure 6.

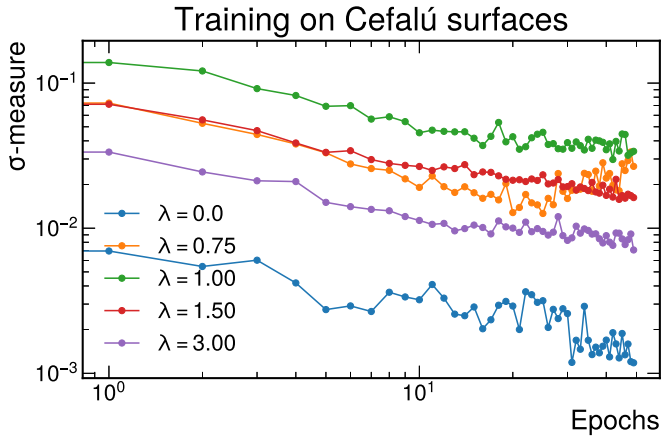

Figure 6. Evolution of the σ loss when training at $\lambda = \lambda^\sharp$. The σ-measure is evaluated on validation set.

4.1.1. $\lambda = 0$. We first consider the smooth K3 obtained from turning off the Cefalú deformation. This supplies a reference point with which to compare calculations on the singular K3 spaces corresponding to the special values $\lambda = \lambda^\sharp \in \{3/4, 1, 3/2, 3\}$. The distribution of the values of c_1^2 is shown on the Figure 7. There we see a widespread distribution for the Fubini–Study metric curvature distribution, while for the trained metric the curvature density concentrates in a sharp peak around zero, as expected for a flat metric.

Also notice in Figure 8 the Euler density distribution for the learned metric is positive at all points, in accordance to the Bogolomov-Yau inequality.

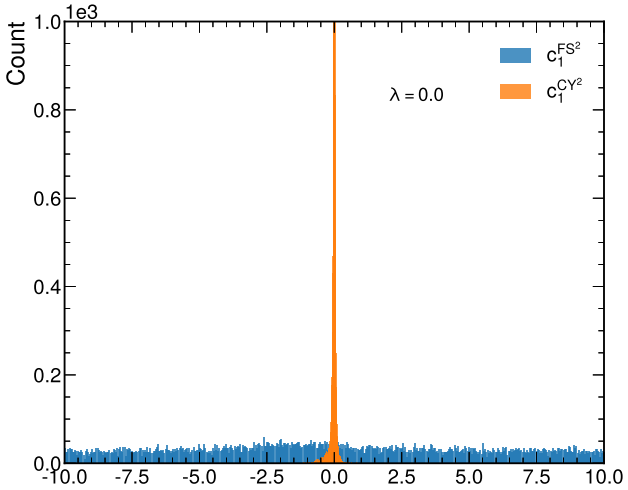

Figure 7. Distribution of the values of c_1^2 using both Fubini–Study and machine learned Calabi–Yau metrics for the Fermat quartic.

Similarly, the distribution of the values of c_2 is shown on the Figure 8.

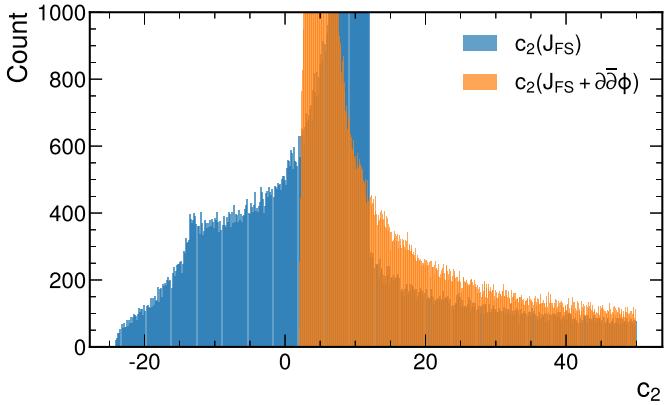

Figure 8. Distribution of the values of c_2 using both Fubini–Study and machine learned Calabi–Yau metrics for the Fermat quartic.

The integral of the Euler density gives the following values:

$$\int_{X_0} c_2(J_0^{\mathrm{FS}}) \approx 24.23\,, \qquad \int_{X_0} c_2(J_0^{\mathrm{CY}}) \approx 24.04\,, \tag{39}$$

where the integral is approximated using 60,000 points.

4.1.2. $\lambda = 3/4$. The number of points in the singular locus Sing $X_{3/4}$ is 8. The singular points of $X_{3/4}$ are of form:

$$\text{Sing } X_{3/4} = \{[\pm 1 : \pm 1 : \pm 1 : \pm 1], \quad \dots\} \ . \tag{40}$$

We consider a small deviation from $\lambda = 3/4$ by considering varieties $X_{3/4\pm\epsilon}$ for some sufficiently small $\epsilon > 0$. This allows us to study the behavior of the Ricci-flat metric and the curvature thereof as we approach $X_{3/4}$. In particular, by observing the histogram of the Euler density on Figure 9, we see that the varieties are not uniformly curved. The histograms highlight the contrast between the Fubini–Study and machine learned curvature distributions. A persistent feature is the positivity of the curvature for the machine learned flat approximation. Naïvely, this should be expected from the Bogolomov–Yau inequality, because a nearly Ricci-flat metric must have $c_1(J)^2$ close to zero. This feature is persistent for all values of λ considered in this work. Let us now explore the curvature tails, *i.e.*, the high curvature

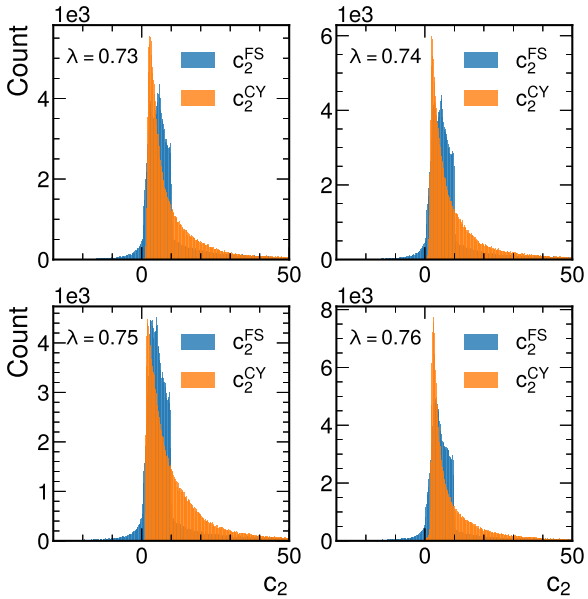

Figure 9. Distribution of the values of the Euler density $e(J_{3/4\pm\epsilon})$ using both $J^{\mathsf{FS}}_{3/4\pm\epsilon}$ and $J^{\mathsf{CY}}_{3/4\pm\epsilon}$.

regions. In particular, let $e(J_{3/4\pm\epsilon})$ denote the Euler density corresponding to the curvature form $J_{3/4\pm\epsilon}$ and consider a subset of $X_{3/4\pm\epsilon}$ defined by a one parameter family:

$$X^{\delta}_{3/4\pm\epsilon} := \{p \in X_{3/4\pm\epsilon} \mid |e(J_{3/4\pm\epsilon})(p)| \geq \delta\}\,, \tag{41}$$

where the cut-off parameter $\delta \in \mathbb{R}$ for the Euler density limits to the high curvature regions in X_λ. The motivation for defining δ is to construct a multi-parameter persistent homology, with δ controlling the cut-off of curvature. We observe that there exists a sufficiently large value of $\delta > 0$ and sufficiently small value of $\epsilon > 0$ such that that the high curvature regions become disconnected in $X^{\delta}_{3/4\pm\epsilon}$.

To study the high Euler density regions, we consider zeroth persistent homology groups $H^r_0(X^{\delta}_{3/4\pm\epsilon})$. In this expression, r is the filtration parameter, *i.e.*, the radius of the sphere around each point on the Calabi–Yau, δ is the lower cutoff of the curvature, and ϵ is the displacement from the singular locus $\lambda = 3/4$ in complex structure moduli space.

Hence, the high curvature regions close to the singularity are at $\delta \gg 1$ and $0 < \epsilon \ll 1$. For $\lambda = 3/4$, we chose $\epsilon = 0.02$ and normalized $\delta = 0.5$ (normalization is such that the value of 1 corresponds to the maximum value of Euler density), and computed the filtration in the range $0 \leq r \leq 2$. For larger values of r, the persistence diagram of $H^r_0(X^{\delta}_{3/4\pm\epsilon})$ has stabilized to a single connected component.

For simplicity, we compute the persistent homology in each patch separately using the Euclidean metric. Specifically, we cover the ambient space $\mathbb{P}^3$ by sets $D_i = \{z_i \neq 0\}$ and consider homology groups of $X^{\delta}_{3/4\pm\epsilon} \cap D_i$. For $\epsilon = 0$, using (40), note that there are total of 8 singular points in each such intersection. In order to ensure that the variety admits well-defined Ricci-flat metric, we consider non-zero $\epsilon > 0$. Thus, the number of generators for different values of $\delta > 0$ at different points in the filtration at $\lambda = 0.73$ is shown in Figure 10 whereas, the persistence barcode for some sufficiently large $\delta > 0$ (in the sense as defined above) is shown in Figure 11. There, for each patch D_i, we observe 8 cycles with large persistence, each corresponding to some neighborhood of a point $p \in \text{Sing } X_{3/4}$. Typical points in each cycle are shown in the Table 3 and are thus consistent with points in Sing $X_{3/4}$.

4.1.3. $\boldsymbol{\lambda = 1}$. The number of points in the singular locus Sing X_1 is 16. The singular points of X_1 are of form:

$$\text{Sing } X_1 = \{[\pm1 : \pm1 : \pm1 : 0],\ [\pm1 : \pm1 : 0 : \pm1],\ \dots\}\ . \tag{42}$$

Patch	Point	Closest point in Sing $X_{3/4}$
D_0	$[1.0 : 0.87 : -0.93 : -0.84]$	$[1 : 1 : -1 : -1]$
	$[1.0 : -0.86 : -0.83 : 0.96]$	$[1 : -1 : -1 : 1]$
	$[1.0 : -0.82 : -0.87 : -0.82]$	$[1 : -1 : -1 : -1]$
	$[1.0 : -0.95 : 0.98 : 0.95]$	$[1 : -1 : 1 : 1]$
	$[1.0 : -0.95 : 0.80 : -0.87]$	$[1 : -1 : 1 : -1]$
	$[1.0 : 0.97 : -0.95 : 0.98]$	$[1 : 1 : -1 : 1]$
	$[1.0 : 0.84 : 0.91 : 0.96]$	$[1 : 1 : 1 : 1]$
	$[1.0 : 0.92 : 0.82 : -0.89]$	$[1 : 1 : 1 : -1]$

Table 3. Typical points in each of the large persistence cycle of $H_0^r(X_{0.73}^\delta \cap D_0)$.

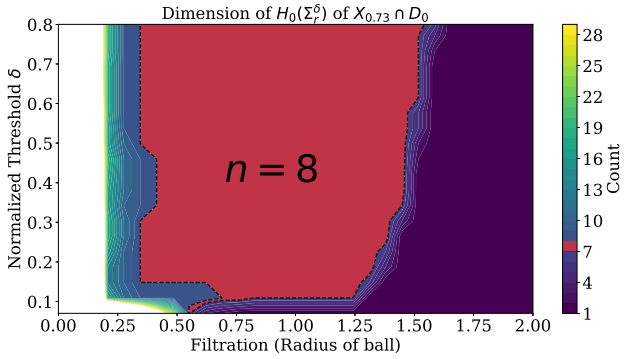

Figure 10. Dimension of $H_0(\Sigma_r^\delta)$ for different values of $\delta > 0$, where Σ_r^δ is a Vietoris–Rips filtration of $X_{0.73}^\delta \cap D_0$. Notice sharp jump in persistence (difference between death and birth indices in Vietoris–Rips filtration) of $n = 8$ generators. The normalized threshold δ is such that normalized $\delta = 1$ corresponds to the largest value of the Euler density.

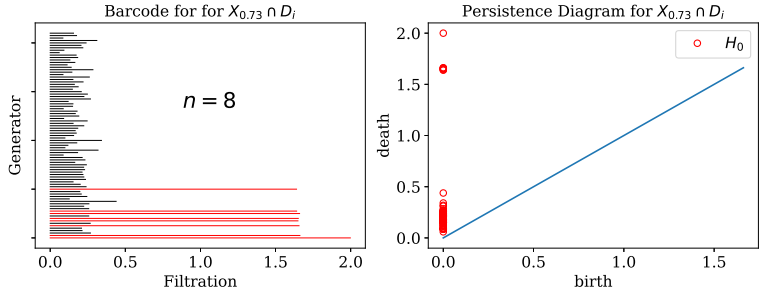

Figure 11. Persistence barcode and diagram of $H_0^r(X_{0.73}^\delta \cap D_0)$ where $D_0 = \{z_0 \neq 0\}$. The number n indicates the number of generators γ with persistence $\mathrm{pers}(\gamma) > 0.7$ (colored as red).

Similarly as in Section 4.1.2, we contemplate deviations from $\lambda = 1$ by considering manifolds $X_{1\pm\epsilon}$ for some sufficiently small $\epsilon > 0$. Histograms of the Euler density $e(J_{1\pm\epsilon})$ for the Fubini–Study metric as well as the machine learned approximation are shown in Figure 12. Similarly, we see that $X_{1\pm\epsilon}$ is not uniformly curved, thus, we consider $X^{\delta}_{1\pm\epsilon}$ defined similarly as a one parameter family:

$$X^{\delta}_{1\pm\epsilon} := \{p \in X_{1\pm\epsilon} \mid |e(J_{1\pm\epsilon})(p)| \geq \delta\}\,. \tag{43}$$

The threshold parameter $\delta \in \mathbb{R}$ is not necessarily the same as in Section 4.1.2. For studying the high Euler density regions, we analogously consider persistent homology groups $H^r_0(X^{\delta}_{1\pm\epsilon} \cap D_k)$ for each patch D_k. For $\epsilon = 0$, each patch contains: $3 \times 2^2 = 12$ singular points. The persistence barcode at $\lambda = 0.98$ is shown in Figure 13. For each patch D_i, we observe 12 cycles with

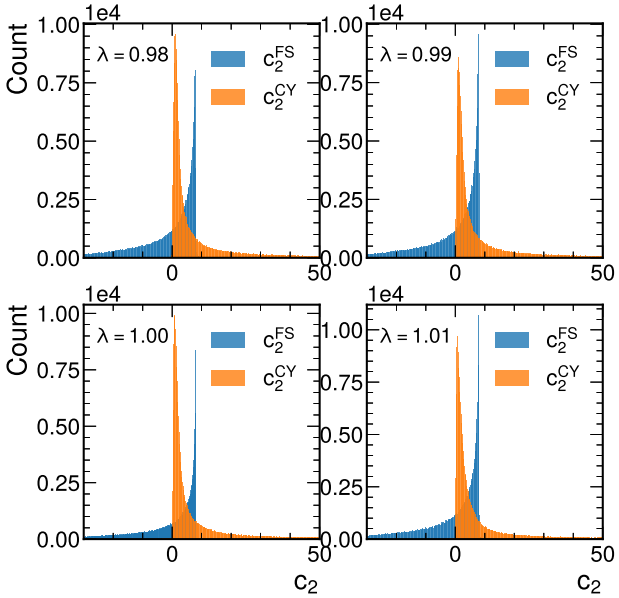

Figure 12. Distribution of the values of the Euler density $e(J_{1\pm\epsilon})$ using both $J^{\mathsf{FS}}_{1\pm\epsilon}$ and $J^{\mathsf{CY}}_{1\pm\epsilon}$.

large persistence, each corresponding to some neighborhood of a point $p \in \operatorname{Sing} X_1$. Typical points in each cycle are shown in Table 4 and are thus also consistent with the points (42) in $\operatorname{Sing} X_1$.

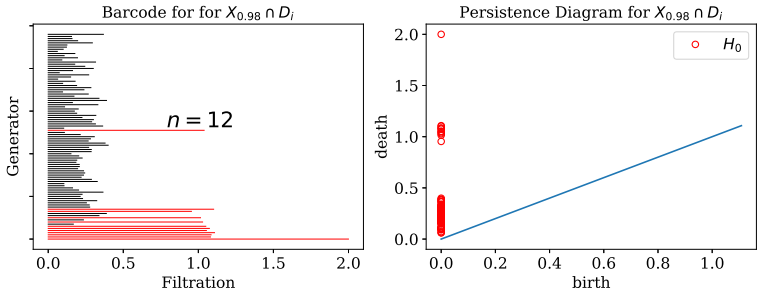

Figure 13. Persistence barcode of $H_0^r(X_{0.98}^\delta \cap D_0)$ where $D_0 = \{z_0 \neq 0\}$. The number n indicates the number of generators γ with persistence $\text{pers}(\gamma) > 0.7$ (colored as red).

.

Furthermore, note that the Euler density $e(J^{\mathsf{CY}}_{1\pm\epsilon})$ also satisfies the same positivity property as $X_{3/4}$, that is: $e(J^{\mathsf{CY}}_{1\pm\epsilon}) \gtrsim 0$, even in the case when $\epsilon = 0$.

Patch	Point	Closest point in Sing X_1
D_0	$[1. : -0.96 : \ 0.97 : \ 0.04]$	$[1 : -1 : \ 1 : \ 0]$
	$[1. : \ 0.98 : \ 0.95 : \ 0.04]$	$[1 : \ 1 : \ 1 : \ 0]$
	$[1. : -0.05 : -0.99 : \ 0.95]$	$[1 : \ 0 : -1 : \ 1]$
	$[1. : \ 0.85 : \ 0.22 : \ 1.]$	$[1 : \ 1 : \ 0 : \ 1]$
	$[1. : -0.92 : \ 0.02 : -0.97]$	$[1 : -1 : \ 0 : -1]$
	$[1. : -0.19 : \ 0.86 : -0.99]$	$[1 : \ 0 : \ 1 : -1]$
	$[1. : \ 0.19 : -0.99 : -0.86]$	$[1 : \ 0 : -1 : -1]$
	$[1. : \ 0.90 : -0.03 : -0.91]$	$[1 : \ 1 : \ 0 : -1]$
	$[1. : -0.99 : -0.96 : -0.08]$	$[1 : -1 : -1 : \ 0]$
	$[1. : \ 0.15 : \ 0.88 : \ 0.98]$	$[1 : \ 0 : \ 1 : \ 1]$
	$[1. : 0.96 : -0.85 : -0.16]$	$[1 : \ 1 : -1 : \ 0]$
	$[1. : -0.94 : -0.10 : \ 0.98]$	$[1 : -1 : \ 0 : \ 1]$

Table 4. Typical points in each of the large persistence cycle of $H_0^r(X_{0.98}^\delta \cap D_0)$.

4.1.4. $\lambda = 3/2$. The number of points in the singular locus Sing $X_{3/2}$ is 12. The singular points of $X_{3/2}$ are of form:

$$\text{Sing } X_{3/2} = \{[\pm 1, \pm 1, 0, 0], \ \dots\} \ . \tag{44}$$

Similarly, we consider deviation from $\lambda = 3/2$ by considering $X_{3/2\pm\epsilon}$ for some sufficiently small $\epsilon > 0$. The histogram of the Euler density $e(J_{3/2\pm\epsilon})$ is shown in Figure 14. For each k, the patch $X_{3/2} \cap D_k$ contains total of

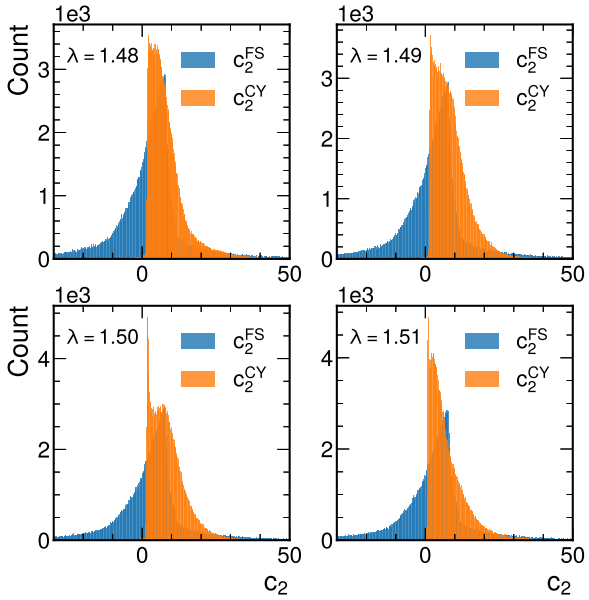

Figure 14. Distribution of the values of the Euler density $e(J_{3/2\pm\epsilon})$ using both $J^{\mathsf{FS}}_{3/2\pm\epsilon}$ and $J^{\mathsf{CY}}_{3/2\pm\epsilon}$.

$3 \times 2 = 6$ singular points. The persistence barcode for $X^{\delta}_{1.48} \cap D_0$ is shown in Figure 14. For each patch D_i we observe 6 cycles with large persistence,

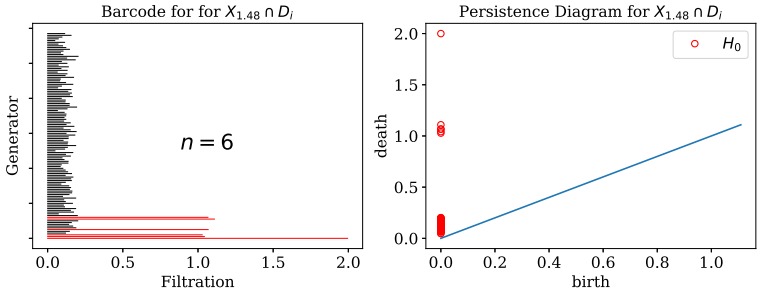

Figure 15. Persistence barcode of $H^r_0(X^{\delta}_{1.48} \cap D_0)$ where $D_0 = \{z_0 \neq 0\}$. The number n indicates the number of generators γ with persistence $\mathrm{pers}(\gamma) > 0.7$ (colored as red).

.

each corresponding some neighborhood of a point $p \in \mathrm{Sing}\ X_{3/2}$. Typical

points in each cycle are shown in the Table 5 and are consistent with the points (44).

Patch	Point	Closest point in Sing $X_{3/2}$
D_0	$[1. : 0.04 : -0.96 : 0.15]$	$[1 : 0 : -1 : 0]$
	$[1. : -0.97 : -0. : 0.06]$	$[1 : -1 : 0 : 0]$
	$[1. : 0.93 : 0.11 : 0.03]$	$[1 : 1 : 0 : 0]$
	$[1. : -0.06 : -0.01 : 0.96]$	$[1 : 0 : 0 : 1]$
	$[1. : -0.02 : 0.90 : -0.14]$	$[1 : 0 : 1 : 0]$
	$[1. : 0.17 : 0.04 : -1.]$	$[1 : 0 : 0 : -1]$

Table 5. Typical points in each of the large persistence cycle of $H_0^r(X^\delta_{1.48} \cap D_0)$.

4.1.5. $\lambda = 3$. The number of points in the singular locus Sing X_3 is 4. The singular points of X_3 are of form:

$$\text{Sing } X_3 = \{[1:0:0:0],\ [0:1:0:0],\ \dots\}\ . \tag{45}$$

Similarly, we consider deviation from $\lambda = 3$ by considering X_3 for sufficiently small $\epsilon > 0$. The histogram of the Euler density $e(J_{3\pm\epsilon})$ is shown in Figure 16. For each k, the patch $X_3 \cap D_k$ contains only a single singular point, thus, instead we consider the persistence barcode of $X^\delta_{2.98}$, shown on the Figure 17.

Point	Closest point in Sing X_3
$[0.04 : -0.03 : 1. : -0.07]$	$[0 : 0 : 1 : 0]$
$[0.03 : -0.10 : 0.08 : 1.]$	$[0 : 0 : 0 : 1]$
$[1. : 0.06 : 0.01 : 0.0]$	$[1 : 0 : 0 : 0]$
$[0.00 : 1. : 0.04 : -0.05]$	$[0 : 1 : 0 : 0]$

Table 6. Typical points in each of the large ($\text{pers}(\gamma) > 0.7$) persistence cycle of $H_0^r(X^\delta_{2.98})$.

The typical points in each large persistence generator of $H_0^r(X_{2.98})$ are shown in Table 6, which is consistent with the singular locus (45).

4.1.6. Asymptotics near large Euler density regions. In the previous sections we have considered the large curvature regions in the vicinity of the singularities for the various $X_{\lambda^\sharp}$ in the Cefalú pencil. Taking points in $X_{\lambda^\sharp \pm \epsilon}$ with a given curvature density $e(J)$ larger than a given parameter t,

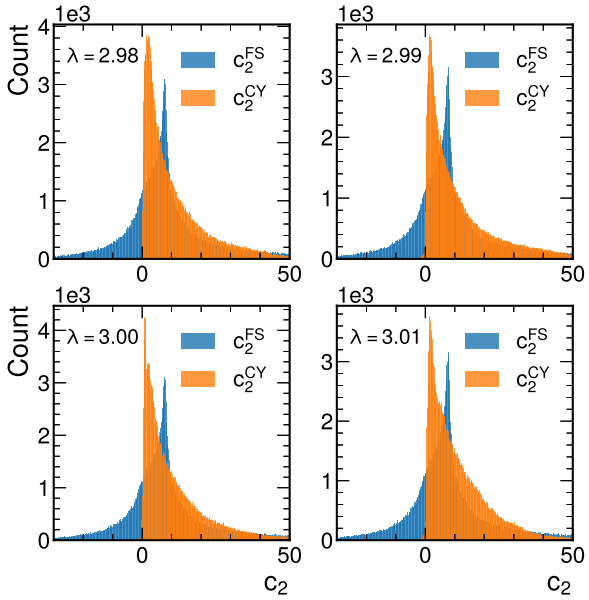

Figure 16. Distribution of the values of the Euler density $e(J_{3\pm\epsilon})$ using both $J^{\mathsf{FS}}_{3\pm\epsilon}$ and $J^{\mathsf{CY}}_{3\pm\epsilon}$.

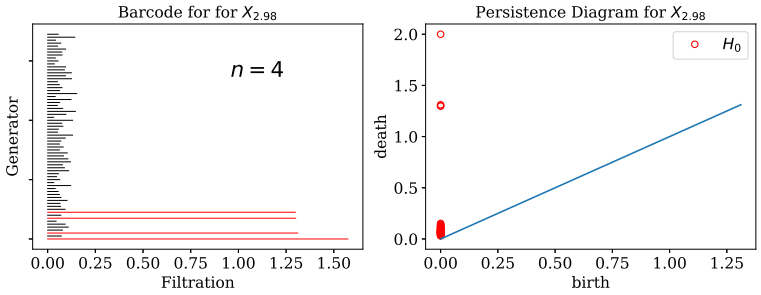

Figure 17. Persistence barcode of $H^r_0(X^\delta_{2.98})$. The number n indicates the number of generators γ with persistence $\mathrm{pers}(\gamma) > 0.7$ (colored as red).

we managed to identify a clustering of points consistent with the singularity distribution for $X_{\lambda^\sharp}$. In addition to the Euler density $c_2(J_\lambda)$, we may also consider $c_1(J_\lambda)^2$. The top forms $c_2(J_\lambda)$ and $c_1(J_\lambda)^2$ induce filtrations of X_λ

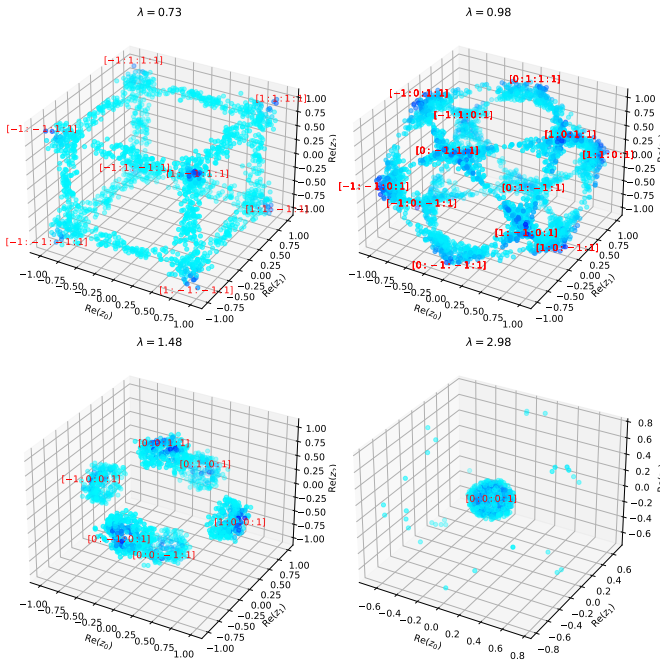

Figure 18. Projection of $X_{\lambda^\sharp+\epsilon,t} \cap D_3$ to $(\mathrm{Re}(z_0),\ \mathrm{Re}(z_1),\ \mathrm{Re}(z_2))$ for some large $t > 0$. The shading is induced by the Euler density: $e(J_{\lambda^\sharp+\epsilon})$. The red labels indicate the singular points of $X_{\lambda^\sharp} \cap D_3$.

.

defined by:

$$X^1_{\lambda,t_1} := \left\{p \in X_\lambda \mid \left|c_1(J_\lambda)^2(p)\right| < t_1\right\}\ ,$$
$$X^2_{\lambda,t_2} := \left\{p \in X_\lambda \mid \left|c_2(J_\lambda)(p)\right| < t_2\right\}\ . \tag{46}$$

To better visualize the occurrence of large curvature values, we pick a patch $D_3 = \{z_3 \neq 0\}$ and for all $\lambda^\sharp$ we construct the scatter plots of $X_{\lambda,t} \cap D_3$, by projecting each point $p = [z_0 : z_1 : z_2 : 1] \in X_{\lambda,t}$ to $(\mathrm{Re}(z_0), \mathrm{Re}(z_1), \mathrm{Re}(z_2))$. This allows us to visualize the clustering behavior observed in the persistence diagrams shown on Figures 11, 13, 15 and 17. We pick values of λ to be $\lambda^\sharp + \epsilon$ for some small $|\epsilon| > 0$ and pick sufficiently large threshold $t > 0$ to highlight the clustering behavior. The results of this are shown on Figure 18. We also include similar plots of the curvature on for the real parts of X_λ in the Figures 19 and 20. Using the definitions for X^1_{λ,t_1} and X^2_{λ,t_2},

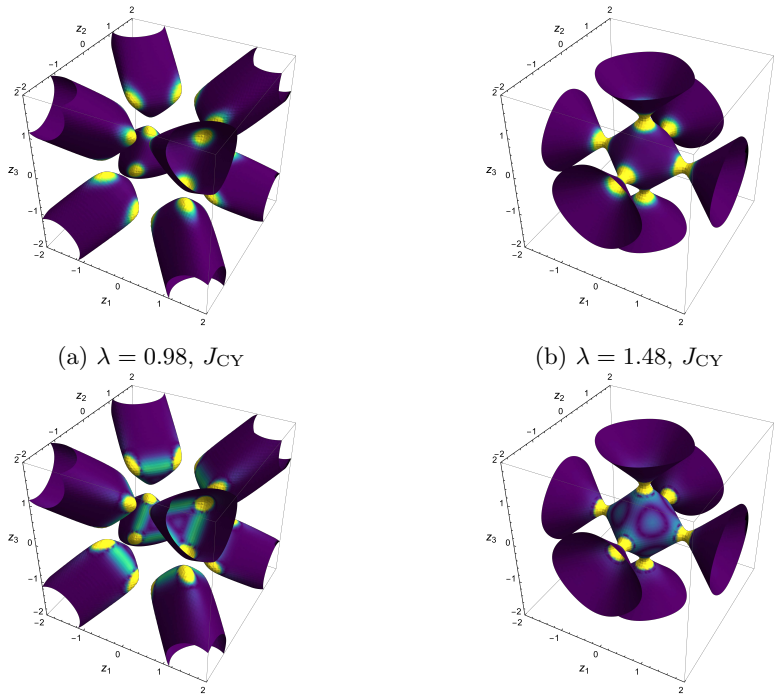

(a) $\lambda = 0.98$, J_{CY} (b) $\lambda = 1.48$, J_{CY}

(c) $\lambda = 0.98$, J_{FS} (d) $\lambda = 1.48$, J_{FS}

Figure 19. Plot of $X_{\lambda^\sharp} \cap D_3 \cap \mathbb{R}^3$ with shading induced by the Euler density. Brighter colors denote larger value of $e(J)$. In order to correctly take into account the identification $\lambda p \sim p$ for $\lambda \in \mathbb{C}^\times$, we have used spectral networks to compute ϕ (See 4.3).

we may study the asymptotic behavior of F_1 and F_2 defined by:

$$F_1(t_1) := \int_{X^1_{\lambda,t_1}} c_1(J_\lambda)^2 \quad \text{and} \quad F_2(t_2) := \int_{X^2_{\lambda,t_2}} c_2(J_\lambda)\,. \tag{47}$$

The numerical result for F_2 is shown on Figure 21. As can be observed from Figure 21, the F_2^{FS}, corresponding to the Fubini–Study metric, converges to the values shown in Table 2, whereas F_2^{CY} seems to converge in all cases with the exception of $\lambda = 1$. Comparing to the learning curves in Figure 6, we see that $\lambda = 1$ exhibits the poorest training (*i.e.*, highest sigma loss). We must also highlight the case of $\lambda = 3$ as it gives the best results in terms of convergence and also yields the smallest loss among the singular models, this can be due to the fact that we have the smallest number of high curvature regions for $\lambda = 3$.

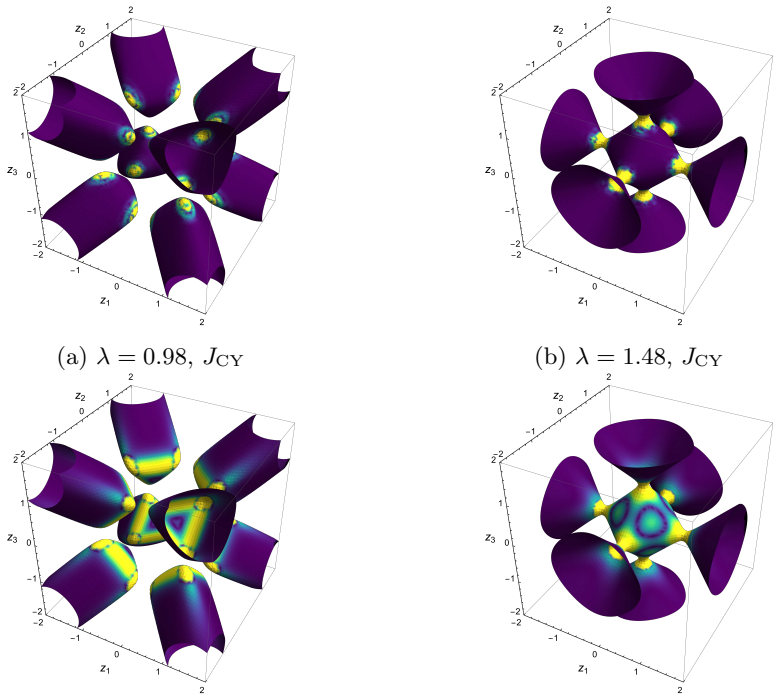

(a) $\lambda = 0.98$, J_{CY} (b) $\lambda = 1.48$, J_{CY}

(c) $\lambda = 0.98$, J_{FS} (d) $\lambda = 1.48$, J_{FS}

Figure 20. Plot of $X_{\lambda^\sharp} \cap D_3 \cap \mathbb{R}^3$ with shading induced by the c_1^2. Brighter colors denote larger value of $c_1^2(J)$. In order to correctly take into account the identification $\lambda p \sim p$ for $\lambda \in \mathbb{C}^\times$, we have used spectral networks to compute ϕ (See 4.3).

Similar behavior can be observed with F_1, for which the result of numerical computation is shown on Figure 22. As it can be seen in that figure, the quantity F_1 computed using the machine learned metric becomes unstable and diverges once normalized $\log(1+t)$ is greater than 0.5. Observing the histogram on Figure 23 corresponding to c_1^2 shows a similar disagreement: the Fubini–Study and Calabi–Yau metric produce different results.

As a cautionary note, we observe that local data derived from the metric, such as the extent to which the Monge–Ampère equation is satisfied pointwise, does not necessarily indicate whether the metric is able to reliably recover global, topological properties of X. Therefore, such local quantities may be unable to provide a complete diagnostic of the phenomenological suitability of the metric.

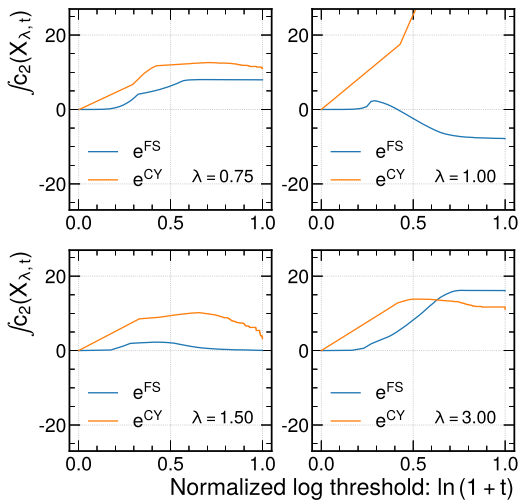

Figure 21. Asymptotic behavior of F_2 for both Fubini–Study and Calabi–Yau metrics.

.

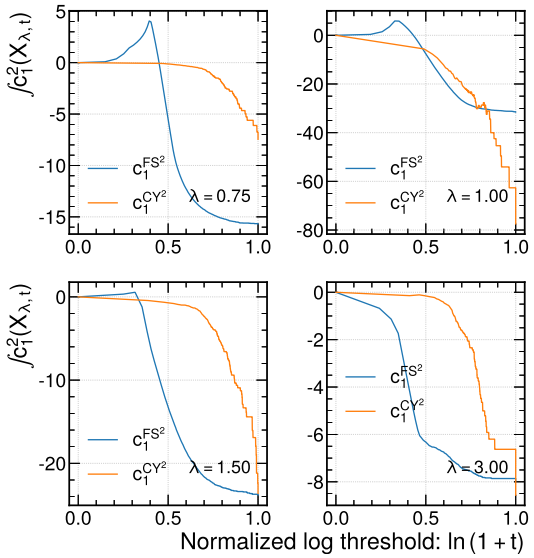

Figure 22. Asymptotic behavior of F_1 for both Fubini–Study and Calabi–Yau metrics.

.

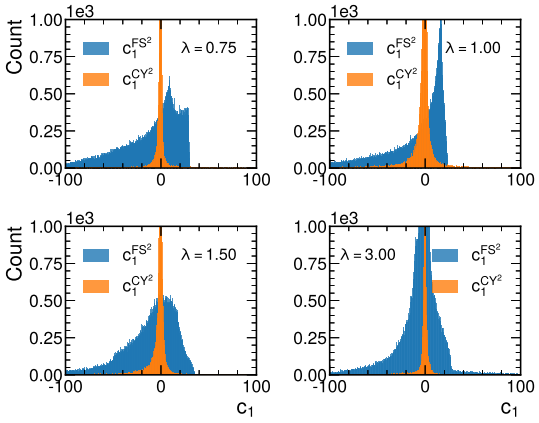

Figure 23. Distribution of the values of $c_1(J_\lambda)^2$ using both J_λ^{FS} and J_λ^{CY}.

.

4.2. Dwork quintic

Similarly to the Dwork quartic, the Dwork quintic can be defined as a 1-parameter family of Calabi–Yau threefolds:

$$Z_\psi = \left\{ \sum_{i=0}^{4} z_i^5 - 5\psi \prod_{i=0}^{4} z_i = 0 \right\} \subseteq \mathbb{P}^4_{\mathbb{C}} \,. \tag{48}$$

Recall that the Dwork quintic family is singular iff the complex structure parameter $\psi \in \mathbb{C}$ is a 5-th root of unity.

We may generalize Proposition 1 to n-folds with isolated A_1 singularities as follows:

Proposition 2. *Let $X \subseteq \mathbb{P}^m$ be a possibly singular projective variety with curvature form J defined on the smooth locus X_s of X. If $|\mathrm{Sing}\ X| < \infty$ and the singularities have type A_1, then:*

$$\int_{X_s} e(J) = \deg c_F(X) - 2(-1)^{\dim X} |\mathrm{Sing}\ X| \,. \tag{49}$$

Proof.

$$\begin{aligned} \int_{X_s} e(J) &= \chi(X) - (-1)^{\dim X} |\mathrm{Sing}\ X| \\ &= \deg c_F(X) - 2(-1)^{\dim X} |\mathrm{Sing}\ X| \,. \end{aligned} \tag{50}$$

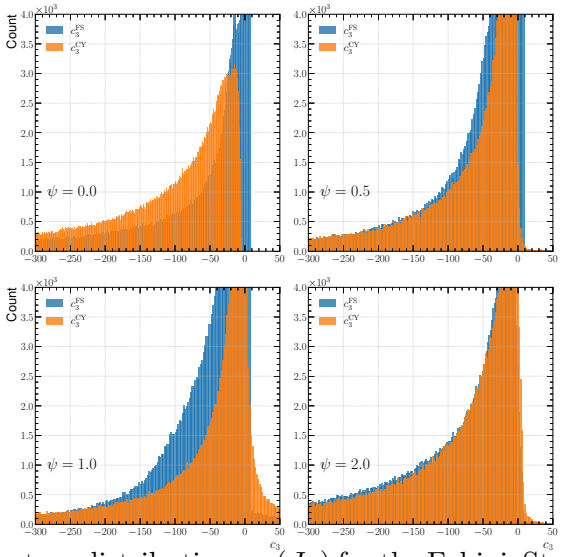

Figure 24. Curvature distributions $c_3(J_\psi)$ for the Fubini–Study and machine learned metric approximations. These distributions were obtained with the `JAX` implementation.

□

Similarly as for Cefalú/Dwork quartic pencils, we consider the histograms of different possible top forms generated by the products of the characteristic forms. The histograms are shown on Figure 25.

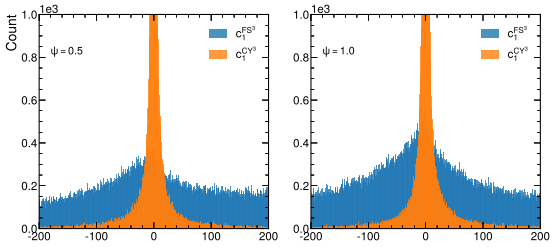

Figure 25. Distribution of the values of the c_1^3 for both J_ψ^{FS} and J_ψ^{CY} at $\psi \in \{1/2,\ 1\}$.

4.2.1. Toric quintic vs. CICY quintic. There are 7,890 Calabi–Yau threefolds realized as complete intersections of polynomial equations in products of projective space [61]. Some of these are also Calabi–Yau hypersurfaces in toric varieties obtained from triangulations of reflexive polytopes in

the Kreuzer–Skarke list [20]. The quintic in $\mathbb{P}^4$ is one such geometry with a double description. Thus, we can calculate a numerical Ricci-flat metric using `cymetric` by considering this manifold in either language. The machine learned metric as a complete intersection Calabi–Yau (CICY) is better than the one obtained from the toric description, where in the latter a random choice of coefficients is used for the degree five defining equation, which is consistent with the general observation that the accuracy of the numerical method is significantly dependent on the choice of a point in the complex structure moduli space.

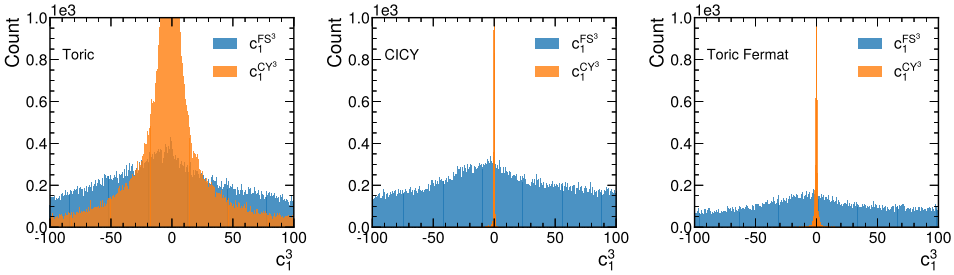

Figure 26. Distribution of curvature densities c_1^3 for the toric quintic with random choice of coefficients on the left, CICY Fermat quintic ($\psi = 0$) in the middle, and toric quintic at the same point in complex structure moduli as Fermat quintic on the right.

Indeed, by fixing the coefficients to be the same as that of the Fermat quintic, we see that the histogram for c_1^3, shown on the right in Figure 26, is similar to that of CICY Fermat quintic shown in the middle in Figure 26.

Type	$\deg c_3(J)$	$\deg c_1(J) \wedge c_2(J)$	$\deg c_1(J)^3$
ToricFS	-183.87	16.24	16.58
Toric	-193.46	11.31	8.27
QuinticFS	-196.43	1.28	-0.28
Quintic	-203.55	0.09	0.00

Table 7. Values of the integrals of the possible top characteristic forms for threefold. The integrals were evaluated using MC integration with $100,000$ points.

4.3. Epilogue: Globally defined ϕ-models and spectral neural networks

Note that the neural network architecture described above does not define a global smooth function $\phi\colon X \to \mathbb{R}$. This in turn implies that $J^{\rm CY}$ and $J^{\rm ref}$ are not necessarily in the same Kähler class under the Ansatz $J^{\rm CY} = J^{\rm ref} + \partial\overline{\partial}\phi$, in fact, $J^{\rm CY}$ might not even be well-defined. We observe this discrepancy by numerically studying the global topological characteristics of $(X, J^{\rm CY})$. In particular, from Figure 4, it is evident that the numerical computation of the topological Euler characteristic $\chi(X)$, computed using (51) deviates significantly from the expected value of $\chi(X) = 24$ for non-singular X.

$$\chi(X) = \int_X {\rm Pf}(J^{\rm CY}) \approx \frac{(-2i)^2}{2!}\frac{1}{N}\sum_{i=1}^{N}\frac{w(p_i)c_2(p_i)}{(\Omega\wedge\overline{\Omega})(p_i)}\,. \tag{51}$$

Furthermore, note that if ϕ had been a global function on X, then, the difference of Pfaffians must be exact [62, 63]:

$${\rm Pf}(J^{\rm CY}) - {\rm Pf}(J^{\rm ref}) = {\rm d}\,{\rm TPf}(J^{\rm CY}, J^{\rm ref})\,. \tag{52}$$

Thus, the numerical approximation (51) should produce results which are within the expected $\chi(X) = 24$ within the margin of the error of numerical integration error.

Recently there has been some progress in designing $\mathbb{C}$-homogeneous and holomorphic neural networks [12, 64]. The idea is to construct pair-wise products of the homogeneous coordinates and apply activation functions which are holomorphic. This allows one to define networks ϕ (called *biholomorphic networks*) such that:

$$\forall\lambda\in\mathbb{C}\colon \phi(\lambda\cdot z) = |\lambda|^{2k}\phi(z)\ , \qquad \text{for some } k\in\mathbb{N}\,. \tag{53}$$

However, although homogeneous, ϕ does not define a global function on X, but a section of $\mathcal{O}_X(k)\otimes\overline{\mathcal{O}_X(k)}$.

Motivated by the observations above, we propose a modified method which allows us to define ϕ to be a global function in $\mathcal{C}^\infty(X)$. To define the setup, let X be a CICY defined as a zero locus of homogeneous polynomials $\{f_i\}_{i=1,\ldots,N}$ where $f_i\in\mathbb{C}[Z_0,\ldots,Z_{n_i}]$, thus X lies in $\mathbb{P}^{n_1}_{\mathbb{C}}\times\cdots\times\mathbb{P}^{n_N}_{\mathbb{C}}$. For each component $\mathbb{P}^{n_i}_{\mathbb{C}}$ of the product, define a mapping:

$$\alpha_{n_i}\colon \mathbb{P}^{n_i}_{\mathbb{C}} \longrightarrow \mathbb{C}^{n_i+1,n_i+1}\,, \tag{54}$$

whose action on a general point $p \in [Z_0 \colon Z_1 \colon \ldots \colon Z_{n_i}] \in \mathbb{P}^{n_i}_{\mathbb{C}}$ is defined as:

$$\alpha_{n_i}(p) = \begin{bmatrix} \frac{Z_0\overline{Z_0}}{|Z|^2} & \frac{Z_0\overline{Z_1}}{|Z|^2} & \cdots & \frac{Z_0\overline{Z_{n_i}}}{|Z|^2} \\ \frac{Z_1\overline{Z_0}}{|Z|^2} & \frac{Z_1\overline{Z_1}}{|Z|^2} & \cdots & \frac{Z_1\overline{Z_{n_i}}}{|Z|^2} \\ \vdots & \vdots & \ddots & \vdots \\ \frac{Z_{n_i}\overline{Z_0}}{|Z|^2} & \frac{Z_{n_i}\overline{Z_1}}{|Z|^2} & \cdots & \frac{Z_{n_i}\overline{Z_{n_i}}}{|Z|^2} \end{bmatrix} . \tag{55}$$

Note that α_{n_i} is a well-defined global smooth function on $\mathbb{P}^{n_i}_{\mathbb{C}}$ and thus its restriction $\alpha_{n_i}|_X$ is a well-defined smooth function on X. Furthermore, note that the components of α_{n_i} correspond to $k_\phi = 1$ basis used in [65] to build the eigenfunctions of Laplace operator Δ, thus we shall refer to the layer of the neural network which applies α_n as a spectral layer and the corresponding neural network - a spectral neural network. We then decompose α_{n_i} into a real and imaginary components:

$$\mathrm{ReIm} \colon \alpha_{n_i}(p) \mapsto (\mathrm{Re} \circ \alpha_{n_i}(p),\ \mathrm{Im} \circ \alpha_{n_i}(p)) \,/\, \text{"redundancies"} . \tag{56}$$

Bearing in mind that α_{n_i} is a Hermitian matrix, we see that $\mathrm{ReIm} \circ \alpha_{n_i}$ is made up of $(n_i+1)^2$ independent real entries. We then define $\rho \colon \mathbb{R}^{\sum_i (n_i+1)^2} \longrightarrow \mathbb{R}$ to be a neural network with d-layers and W_i-nodes in layer $i \in \{1, \ldots, d\}$. Finally, we combine these mappings to define $\phi \colon X \to \mathbb{R}$ as:

$$\phi := \rho \circ \big(\mathrm{ReIm} \circ \alpha_{n_1}|_X,\ \mathrm{ReIm} \circ \alpha_{n_2}|_X,\ \ldots,\ \mathrm{ReIm} \circ \alpha_{n_N}|_X\big) . \tag{57}$$

That ϕ is well-defined on X is trivial, since for all

$$p = ([Z_0^{(1)} \colon \ldots \colon Z_{n_1}^{(1)}], \ldots, [Z_0^{(N)} \colon \ldots \colon Z_{n_N}^{(N)}])$$

in X, and for every $\lambda = (\lambda_1, \ldots, \lambda_N) \in \mathbb{C}^{\times N}$, we have:

$$\begin{aligned} \phi(\lambda \cdot p) &= \phi((\lambda_1 p_1, \ldots, \lambda_N p_N)) \\ &= \rho \circ \big(\mathrm{ReIm} \circ \alpha_{n_1}(\lambda_1 p_1),\ \ldots,\ \mathrm{ReIm} \circ \alpha_{n_N}(\lambda_N p_N)\big) \\ &= \rho \circ \big(\mathrm{ReIm} \circ \alpha_{n_1}(p_1),\ \ldots,\ \mathrm{ReIm} \circ \alpha_{n_N}(p_N)\big) = \phi(p) . \end{aligned} \tag{58}$$

The spectral neural network architecture of ϕ is shown on Figure 27. Note that the spectral networks with 0 hidden layers and $x \mapsto \ln(x)$ activation function are equivalent to algebraic metrics with $k = 1$ [24, 25]. In Figure 28, we present the values for the Euler number obtained using the spectral neural

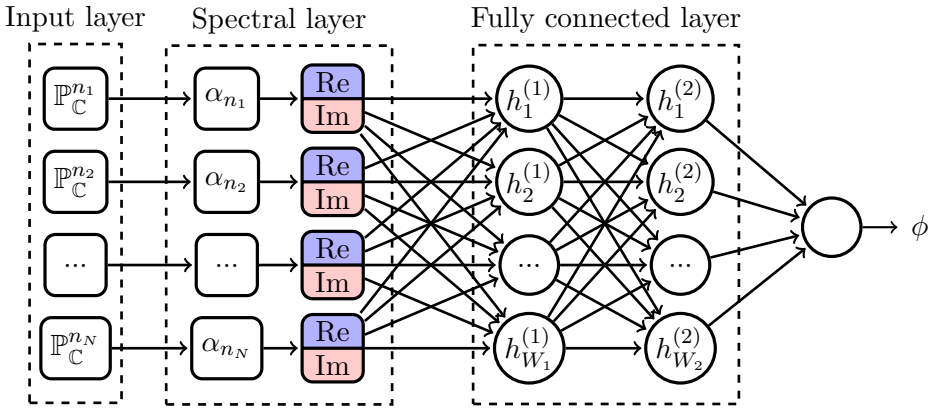

Figure 27. Spectral neural network architecture: Prior to the fully connected neural network we introduce the spectral layer, taking real and imaginary parts of $\mathbb{C}^*$-invariant quantities.

networks. The numerical integrals computed using the spectral networks sketched in Figure 27 are mostly close to the expected Euler characteristic, within the margin of the error due to the Monte Carlo integration.

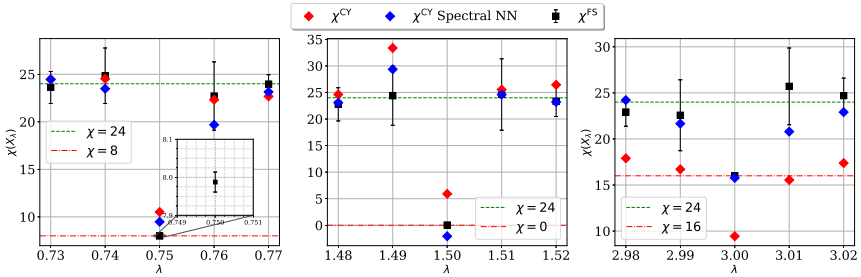

Figure 28. Numerical values of (24) along the Cefalú pencil. Black points and error bars showing a 95% confidence interval are associated to Fubini–Study results, while the red and blue dots correspond to the machine learned metric approximation using fully-connected and spectral networks, respectively. See Appendix A for the details on integration.

The numerical values of (24) along the Cefalú pencil near $\lambda = 1$ are shown on the Figure 29. There are no convergence issues for spectral network Euler number at $\lambda = 1$, in sharp contrast with the fully connected neural network. The convergence plot in shown in Figure 30.

The plots in Figure 30 highlight a sharp contrast among the ϕ-model neural network and the spectral neural network. As one includes points

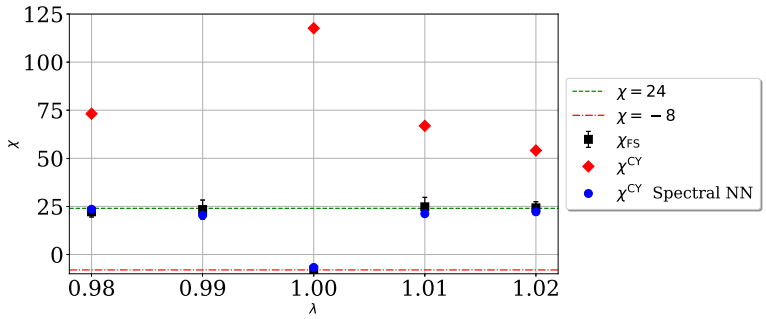

Figure 29. Numerical values of (24) along the Cefalú pencil near $\lambda = 1$. The plot markers are the same as in Figure 4. The value of χ^{CY} using fully-connected network at $\lambda = 0.99$ is off the chart: $\chi^{\mathrm{CY}} \approx 85510$.

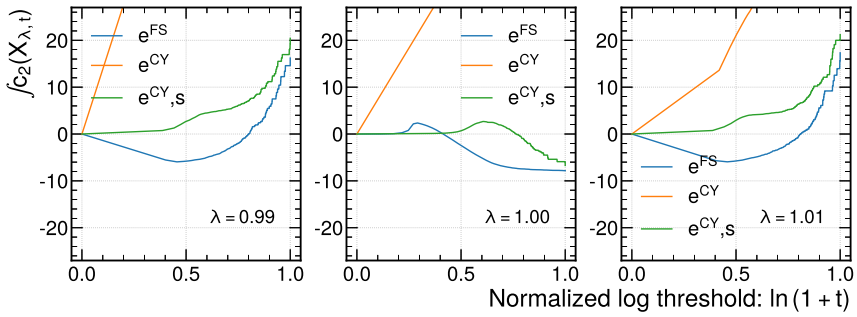

Figure 30. Convergence plot for $c_2(X_\lambda)$ around $\lambda = 1$; the spectral network results (green, "s" subscript) show significant improvement.

λ	$\lvert\mathrm{Sing}\ X\rvert$	deg $c_2(J_\lambda^{\mathrm{FS}})$	deg $c_2(J_\lambda^{\mathrm{CY}})$ w/ Spectral Layer	deg $c_2(J_\lambda^{\mathrm{CY}})$ w/o Spectral Layer
0	0	24	24	24
3/4	8	7.99 ± 0.03	9.48	10.52
1	16	-7.99 ± 0.08	-6.71	117.59
3/2	12	0.0 ± 0.1	-2.07	5.90
3	4	16.00 ± 0.09	15.77	9.44

Table 8. Values of the Monte Carlo approximations of the integrals of $c_2(X_\lambda)$. Note that the results computed using spectral networks are closer to the expected value. The points that were sampled in order to compute above integrals are different than the ones sampled in Figure 4.

close to the singularities, the curvature for the ϕ-model starts diverging.

This suggests that as one approaches the singularity the neural network is not to be trusted. This is not the case for the spectral networks. Here, as one continues adding points to the curvature integral it keeps following the Fubini–Study. In Table 8, we notice that spectral neural networks and Fubini–Study produce similar results for the curvature.

5. Conclusions

In this work we have considered two families of Calabi–Yau manifolds: the Cefalú family of quartics and the more broadly studied Dwork quintic family. For both of these, we have developed the algorithms to compute topological quantities derived from their corresponding Chern characters. This implementation can be easily extended to the whole CICY dataset. Our algorithms utilize some of the neural network approximation models of the `cymetric` package: the so called `PhiModel`. We also employ our own `JAX` implementation of this.

Computation of topological quantities is a crucial fitness check for numerical Calabi–Yau metrics. At first one might think that these relatively straightforward computations automatically work out as they are metric independent. However, one has to bear in mind that the possible neural network approximations constitute a far broader set of solutions than that of globally defined Kähler metrics. Choosing smooth activation functions for the neural network ensures that the metric is smooth over each of the patches. Similarly, if the metric is obtained from the so-called `PhiModel`, over each patch one has $dJ = 0$, satisfying some local form of Kählerity. In the matching of patches, however, it is not guaranteed *a priori* that the perturbation ϕ_{NN} respects the Kähler transformation rules of the seed Kähler potential (in our case, the Fubini–Study potential). That is an inherent issue with these numerical approximations and for the cases in which this situation is non-negligible we expect significant deviations when computing topological quantities.

Deviations from the expected values are not necessarily due to the approximation: they might also be due to the sample size. In the smooth Calabi–Yau cases, we have observed that the neural network approximation to the flat metric behaves well over the entire manifold, and convergence to the right Euler number is achieved. In some of the singular cases, the neural network approximation gives curvature values in the vicinity of the singularities, that once weighted in the Euler number integral produce divergent results. While this is expected, it is also problematic, as increasing the

number of points inevitably brings us close to the singularities, leading ultimately to unacceptable metrics. We notice that these situations can occur in the case of the ϕ-model neural network for some values of λ. As a surprising result, we observe that for the spectral networks, the curvatures near the singularities remain in check and that the global computations match the Fubini–Study results within numerical errors. We observed that for all values of λ considered here there is convergence for the Euler number as one increases the number of points. This suggests that in the singular cases, the spectral neural network is a good generalization of the metric in high curvature regions. The best results were obtained in cases where the number of points used for training is of similar order as the number of points used for the integration.

Spectral networks seem to be able to provide reliable topological data even for singular manifolds. As a proof of principle we demonstrated how the spectral network predictions for the Euler number are within error bars for the Cefalú family of quartics. The spectral networks also lead to smaller sigma losses compared to a standard neural network approximation: As we see in Figure 31, the σ loss for the spectral network at $\lambda = 0$ is below 10^{-3}. This is consistent with the level of accuracy attained for $k = 8$ in [25].

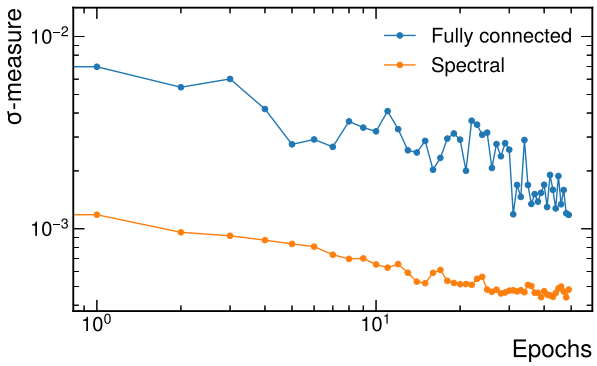

Figure 31. Evolution of σ loss at $\lambda = 0$ using fully-connected and spectral networks indicates a better performance for the latter. The σ loss is evaluated on the validation set. This network is elaborated further in [59].

A globally consistent Calabi–Yau metric must be able to produce the right value for any topological value on the manifold. Having numerical approximations implies having errors in the computation. A natural question is what error values are tolerable and how they can be related to the error

(loss) function in the numerical approximation. Clearly, topological quantities are not sensible to flatness, but as we already highlighted, they are a crucial check for the global consistency of the metric approximation. This global consistency if of utmost importance, particularly in computation of "global" quantities such as the Yukawa couplings for a given string compactification model.

Our work makes use of the `JAX` $\int_Q c_3$, where the third Chern form c_3 is derived from the curvature two-form on a Hermitian manifold. Using a three-layer densely connected neural network with 64 units in each layer as the ϕ-approximant,[10] employing 1024 points in the Monte Carlo integration, this computation takes $387\text{ms} \pm 7.54$ ms using `JAX` compared to $4.41\text{s} \pm 18.3$ ms (mean $\pm$ standard deviation over 7 runs.)

We intend to open source our codebase as a fully-fledged package in a forthcoming publication [59].

Acknowledgments. We thank Carl Henrik Ek, Mario Garcia-Fernandez, Mathis Gerdes, Matt Headrick, and Fabian Ruehle, for helpful discussions, Oisin Kim for critical and instructive suggestions, and Katrin Wendland for discussions on the "≈"-identification subtleties in (2) and in Figure 1. We are grateful to the anonymous referee for helpful and constructive comments on the text. PB would like to thank the Hamilton Institute and Mathematics Department at Trinity College Dublin for their hospitality. GB also wants to thank the 2022 IAIFI Summer School including the computational resources provided through the school. TH is grateful to the Department of Mathematics, University of Maryland, College Park, MD and the Physics Department of the Faculty of Natural Sciences of the University of Novi Sad, Serbia, for the recurring hospitality and resources. PB and GB are supported in part by the Department of Energy grant DE-SC0020220. VJ is supported by the South African Research Chairs Initiative of the Department of Science and Innovation and the National Research Foundation. CM is supported by a Fellowship with the Accelerate Science program at the Computer Laboratory, University of Cambridge. JT is supported by a studentship with the Accelerate Science Program.

[10]The numerical experiments were performed on an Intel 16-Core Xeon Gold 5218 machine with an Nvidia A100 40GB GPU.

Appendix A. Numerical integration

The sampled points are not uniformly distributed with respect to the desired Ricci-flat metric [66, 67]. Instead, the density sampled points ρ is built in such a way that

$$\int_X \mathrm{dVol}_{\mathsf{FS}}\ \rho = 1\,, \tag{A.1}$$

having the condition that the sampled points are uniformly distributed with respect to the Fubini–Study metric $\rho \sim 1/\mathrm{dVol}_{\mathsf{FS}}$, we obtain the following expression

$$\rho = \frac{1}{\mathrm{Vol}_{\mathsf{CY}}}\,\frac{\mathrm{dVol}_{\mathsf{CY}}}{\mathrm{dVol}_{\mathsf{FS}}}\,. \tag{A.2}$$

with $\mathrm{dVol}_{\mathsf{CY}} = \Omega \wedge \bar{\Omega}$. In this fashion, integration of a given function over the Calabi–Yau one obtains

$$\int_X \mathrm{dVol}_{\mathsf{CY}}\ f(z,\bar{z}) = \mathrm{Vol}_{\mathsf{CY}} \int_X \mathrm{dVol}_{\mathsf{FS}}\ f(z,\bar{z})\,\rho\,. \tag{A.3}$$

Let's now consider the integration as a finite sum of N_p points uniformly distributed with respect to the Fubini–Study metric, (A.1) reads

$$\int_X \rho\ \mathrm{dVol}_{\mathsf{FS}} = \frac{\mathrm{Vol}_{\mathsf{FS}}}{N_p}\sum_i \rho(p_i) = 1\,. \tag{A.4}$$

Similarly, (A.3) reads:

$$\begin{aligned}\int_X \mathrm{dVol}_{\mathsf{CY}}\ f(z,\bar{z}) &= \mathrm{Vol}_{\mathsf{CY}}\frac{\mathrm{Vol}_{\mathsf{FS}}}{N_p}\sum_i f(p_i)\,\rho(p_i)\\ &= \frac{\mathrm{Vol}_{\mathsf{CY}}}{\sum_i \rho(p_i)}\sum_i f(p_i)\,\rho(p_i)\,.\end{aligned} \tag{A.5}$$

Special care needs to be taken when dealing with topological quantities, such as

$$\int_X c_3 = \int_X \mathrm{dVol}_{\mathsf{FS}}\ \frac{c_3}{\mathrm{dVol}_{\mathsf{FS}}} = \frac{\mathrm{Vol}_{\mathsf{FS}}}{N_p}\sum_i \frac{c_3}{\mathrm{dVol}_{\mathsf{FS}}}\rho(p_i)\,. \tag{A.6}$$

Using a different expression for the Euler number (from the Chern–Gauss–Bonnet theorem)

$$\chi = \int_X \mathrm{dVol}_g \, K(R_g)\,, \tag{A.7}$$

where $K(R_g)$ is a function of the Riemann tensor. Then if we want to compute the Euler number for the Fubini–Study metric we get:

$$\chi_{\mathsf{FS}} = \frac{\mathrm{Vol}_{\mathsf{FS}}}{N_p} \sum_i K(R_{\mathsf{FS}})\,. \tag{A.8}$$

For the machine learned numerical metric

$$\chi_{\mathsf{ML}} = \frac{\mathrm{Vol}_{\mathsf{FS}}}{N_p} \sum_i K(R_{\mathsf{ML}}) \frac{\mathrm{dVol}_{\mathsf{ML}}}{\mathrm{dVol}_{\mathsf{FS}}}\,. \tag{A.9}$$

Appendix B. Plurisubharmonic property (metric positivity)

In order for $J_\phi = J_{\mathrm{FS}} + \partial\overline{\partial}\phi$ to define a Kähler metric, the corresponding Riemannian metric must be positive definite, that is, $\phi \in C^\infty(X)$ must be J_{FS}-psh function, that is, for every point $p \in X$, there is a neighborhood U of p, s.t. locally $J|_U = \partial\overline{\partial}(\psi + \phi)$, where $\psi + \phi$ is psh on U. Equivalently, ϕ is J_{FS}-psh if we have:

$$J_{\mathrm{FS}} + \partial\overline{\partial}\phi \geq 0\,, \tag{B.10}$$

in the sense of currents. The strict positivity is guaranteed by non-degeneracy of J_ϕ. We may numerically check this, by computing the eigenvalues of the Hermitian matrix of coefficients of J_ϕ. Then, $J_\phi > 0$ iff all of the eigenvalues λ of its matrix of coefficients are positive.

The numerical result for $\lambda = 0.99$ using a spectral network ϕ compared against J_{FS} is shown on Figure B1. We observe a similar positivity of eigenvalues for different values of λ in the Cefalú pencil. However, it must be noted that although this is a necessary condition for ϕ to be J_{FS}-plurisubharmonic, this is not sufficient.

Appendix C. Classical volume terms dominate

As an additional crosscheck we must ensure that the numerical quantities obtained are the most relevant even after including quantum corrections.

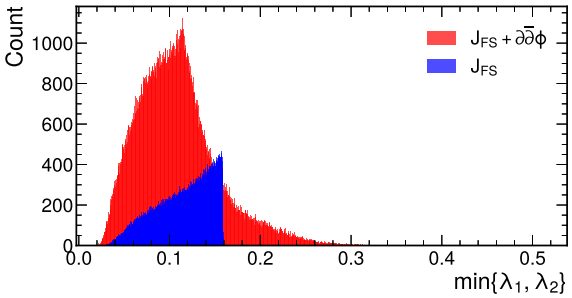

Figure B1. Distribution of the minimum of the eigenvalues over X_λ for $\lambda = 0.99$.

Writing the Kähler form in a basis for $H^{(1,1)}(X,\mathbb{Z})$ as $J = t^i J_i$ we obtain the volume as

$$V = \int_X J \wedge J \wedge J = k_{ijk} t^i t^j t^k \,, \tag{C.11}$$

where k_{ijk} are the triple intersection numbers. Take the Kähler potential for the quintic

$$K(z,\bar{z}) = \frac{t}{2\pi} \log(z\bar{z}) \tag{C.12}$$

in this manner, $J(z,\bar{z}) = tJ_0$, and the volume

$$V = t^3 V_0 \,, \quad V_0 = \int_X J_0 \wedge J_0 \wedge J_0 \,. \tag{C.13}$$

The Kahler potential for the IIB flux compactification on the Calabi–Yau is given (with the first α' corrections is given by [68])

$$\begin{aligned} K = &-2 \log \left(V - \frac{\chi(X)\,\zeta(3)}{4(4\pi)^3 g_s^{3/2}} \right) \\ &- \log(S + \bar{S}) - \log \left(-i \int_X \Omega \wedge \bar{\Omega} \right) . \end{aligned} \tag{C.14}$$

The term $\chi(X)\,\zeta(3)/4(4\pi)^3 g_s^{3/2}$ is the first α' correction term. Note that it does not scale with t as the Euler number is topological. In general, α' does not have a t dependence. Note that $g \sim t$, and hence $g^{-1} \sim t^{-1}$. In this manner, the Christoffel symbols $\Gamma \sim g^{-1}\partial g$ and therefore the Riemann tensors are independent of t.

References

[1] P. Candelas, G. T. Horowitz, A. Strominger and E. Witten, *Vacuum configurations for superstrings*, Nucl. Phys. B **258** (1985), 46–74.

[2] P. Candelas and S. Kalara, *Yukawa couplings for a three generation superstring compactification*, Nucl. Phys. B **298** (1988), 357–368.

[3] M. B. Green, J. Schwarz and E. Witten, Superstring Theory. Vol. 2: Loop Amplitudes, Anomalies and Phenomenology, Cambridge University Press, 1988.

[4] S.-T.Yau, *Calabi's conjecture and some new results in algebraic geometry*, Proceedings of the National Academy of Sciences **74** (1977), 1798–1799.

[5] S.-T.Yau, *On the Ricci curvature of a compact Kähler manifold and the complex Monge-Ampère equation. I.*, Comm. Pure. Appl. Math. **31** (1978), 339–411.

[6] E. Calabi, *The space of Kähler metrics*, Proc. Int. Cong. Math. Amsterdam **2** (1954), 206–207.

[7] S. Kachru, A. Tripathy and M. Zimet, *K3 metrics from little string theory*, `arXiv:1810.10540`.

[8] S. Kachru, A. Tripathy and M. Zimet, *K3 metrics*, `arXiv:2006.02435`.

[9] K. Volkert, Space forms: a history, in The Manifold Atlas, `http://www.map.mpim-bonn.mpg.de/Space_forms:_a_history`.

[10] A. Ashmore, Y.-H. He and B. A. Ovrut, *Machine learning Calabi–Yau metrics*, Fortsch. Phys. **68** (2020) 2000068.

[11] L. B. Anderson, M. Gerdes, J. Gray, S. Krippendorf, N. Raghuram and F. Ruehle, *Moduli-dependent Calabi-Yau and SU(3)-structure metrics from machine learning*, `arXiv:2012.04656`.

[12] M. R. Douglas, S. Lakshminarasimhan and Y. Qi, *Numerical Calabi-Yau metrics from holomorphic networks*, `arXiv:2012.04797`.

[13] V. Jejjala, D. K. Mayorga Pena and C. Mishra, *Neural network approximations for Calabi-Yau metrics*, JHEP **08** (2022) 105.

[14] M. Larfors, A. Lukas, F. Ruehle and R. Schneider, *Learning size and shape of Calabi-Yau spaces*, `arXiv:2111.01436`.

[15] A. Ashmore, L. Calmon, Y.-H. He and B. A. Ovrut, *Calabi-Yau metrics, energy functionals and machine-learning*, arXiv:2112.10872.

[16] M. Larfors, A. Lukas, F. Ruehle and R. Schneider, *Numerical metrics for complete intersection and Kreuzer–Skarke Calabi–Yau manifolds*, Mach. Learn. Sci. Tech. **3** (2022) 035014.

[17] A. Ashmore, *Eigenvalues and eigenforms on Calabi-Yau threefolds*, arXiv:2011.13929.

[18] A. Ashmore and F. Ruehle, *Moduli-dependent KK towers and the swampland distance conjecture on the quintic Calabi-Yau manifold*, Phys. Rev. D **103** (2021) 106028.

[19] M. Larfors, A. Lukas, F. Ruehle and R. Schneider, Cymetric, https://github.com/pythoncymetric/cymetric.

[20] M. Kreuzer and H. Skarke, *Complete classification of reflexive polyhedra in four-dimensions*, Adv. Theor. Math. Phys. **4** (2002), 1209–1230.

[21] S. Donaldson, *Scalar curvature and projective embeddings, I*, J. Differential Geom. **59** (2001), 479–522.

[22] S. K. Donaldson, *Some numerical results in complex differential geometry*, arXiv:0512625.

[23] M. R. Douglas, R. L. Karp, S. Lukic and R. Reinbacher, *Numerical Calabi-Yau metrics*, J. Math. Phys. **49** (2008) 032302.

[24] M. Headrick and T. Wiseman, *Numerical Ricci-flat metrics on K3*, Class. Quant. Grav. **22** (2005), 4931–4960.

[25] M. Headrick and A. Nassar, *Energy functionals for Calabi-Yau metrics*, Adv. Theor. Math. Phys. **17** (2013), 867–902.

[26] W. Cui and J. Gray, *Numerical metrics, curvature expansions and Calabi-Yau manifolds*, JHEP **05** (2020) 044.

[27] M. R. Douglas, *Holomorphic feedforward networks*, Pure Appl. Math. Quart. **18** (2022), 251–268.

[28] M. R. Douglas, R. L. Karp, S. Lukic and R. Reinbacher, *Numerical solution to the Hermitian Yang-Mills equation on the fermat quintic*, JHEP **12** (2007) 083.

[29] V. Braun, T. Brelidze, M. R. Douglas and B. A. Ovrut, *Calabi-Yau metrics for quotients and complete intersections*, JHEP **05** (2008) 080.

[30] V. Braun, T. Brelidze, M. R. Douglas and B. A. Ovrut, *Eigenvalues and eigenfunctions of the scalar laplace operator on Calabi-Yau manifolds*, JHEP **07** (2008) 120.

[31] L. B. Anderson, V. Braun, R. L. Karp and B. A. Ovrut, *Numerical hermitian Yang-Mills connections and vector bundle stability in heterotic theories*, JHEP **06** (2010) 107.

[32] L. B. Anderson, V. Braun and B. A. Ovrut, *Numerical hermitian Yang-Mills connections and Kahler cone substructure*, JHEP **01** (2012) 014.

[33] F. Catanese, *Kummer quartic surfaces, strict self-duality, and more*, `arXiv:2101.10501`.

[34] P. Candelas, X. C. De La Ossa, P. S. Green and L. Parkes, *A Pair of Calabi-Yau manifolds as an exactly soluble superconformal theory*, Nucl. Phys. B **359** (1991), 21–74.

[35] P. Candelas, X. C. De la Ossa, P. S. Green and L. Parkes, *An exactly soluble superconformal theory from a mirror pair of Calabi-Yau manifolds*, Phys. Lett. B **258** (1991), 118–126.

[36] W. Nahm and K. Wendland, *A hiker's guide to K3: Aspects of $N = (4, 4)$ superconformal field theory with central charge $c = 6$*, Commun. Math. Phys. **216** (2001), 85–138.

[37] K. Wendland, *On Superconformal field theories associated to very attractive quartics*, `arXiv:0307066`.

[38] P. Berglund and T. Hübsch, *Hirzebruch surfaces, tyurin degenerations and toric mirrors: bridging generalized Calabi-Yau constructions*, `arXiv:2205.12827`.

[39] M. Reid, *The Du Val singularities A_n, D_n, E_6, E_7, E_8*, `https://homepages.warwick.ac.uk/~masda/surf/more/DuVal.pdf`.

[40] T. Hubsch, Calabi–Yau manifolds: A Bestiary for Physicists, World Scientific, 1992.

[41] M. Atiyah and G. B. Segal, *On equivariant Euler characteristics*, J. Geom. Phys. **6** (1989), 671–677.

[42] P. Candelas, Lectures on Complex Manifolds, World Sci. Publishing, Singapore, 1988.

[43] W. Ballmann, Lectures on Kähler Manifolds, EMS Press, 1st Edition, 2006.

[44] R. D. MacPherson, *Chern classes for singular algebraic varieties*, Annals of Mathematics **100** (1974), 423–432.

[45] P. Aluffi, *MacPherson's and Fulton's Chern classes of hypersurfaces*, International Mathematics Research Notices **1994** (1994), 455–465.

[46] P. Aluffi, *Chern classes for singular hypersurfaces*, Transactions of the American Mathematical Society **351** (1999), 3989–4026.

[47] M. Helmer, *Algorithms to compute the topological Euler characteristic, Chern–Schwartz–MacPherson class and Segre class of projective varieties*, Journal of Symbolic Computation **73** (2016), 120–138.

[48] P. Aluffi, The Chern–Schwartz–MacPherson class of an embeddable scheme, in Forum of Mathematics, Sigma, vol. 7, Cambridge University Press, 2019.

[49] A. Parusinski and P. Pragacz, *Characteristic classes of hypersurfaces and characteristic cycles*, `arXiv:9801102`.

[50] P. Aluffi and M. Goresky, *Pfaffian integrals and invariants of singular varieties*, `arXiv:1901.06312`.

[51] R. Piene, *on polar cycles and Chern classes of singular projective varieties*, Travaux en Cours. **37** (1988).

[52] D. Siersma and M. Tibăr, *Polar degree of hypersurfaces with 1-dimensional singularities*, Topology and its Applications **313** (2022) 107992.

[53] J. Huh, *Milnor numbers of projective hypersurfaces with isolated singularities*, Duke Mathematical Journal **163** (2014), 1525–1548.

[54] S.-T. Yau, *On the Ricci curvature of a compact Kähler manifold and the complex Monge-Ampére equation I*, Communications on Pure and Applied Mathematics **31** (1978), 339–411.

[55] S.-T. Yau, *Calabi's conjecture and some new results in algebraic geometry*, Proceedings of the National Academy of Sciences **74** (1977), 1798–1799.

[56] H. Guggenheimer, *Über vierdimensionale Einsteinräume*, Experientia **8** (1952), 420–421.

[57] X. Roulleau, *On generalized Kummer surfaces and the orbifold Bogomolov-Miyaoka-Yau inequality*, Transactions of the American Mathematical Society **371** (2019), 7651–7668.

[58] J. Bradbury, R. Frostig, P. Hawkins, M. J. Johnson, C. Leary, D. Maclaurin et al., *JAX: composable transformations of Python+NumPy programs*, `http://github.com/google/jax`.

[59] P. Berglund, G. Butbaia, T. Hübsch, V. Jejjala, O. Kim, D. Mayorga Peña et al., Work in progress.

[60] D. R. Grayson and M. E. Stillman, "Macaulay2, a software system for research in algebraic geometry." `http://www.math.uiuc.edu/Macaulay2/`.

[61] P. Candelas, A. Dale, C. Lutken and R. Schimmrigk, *Complete intersection Calabi-Yau manifolds*, Nucl. Phys. B **298** (1988), 493–525.

[62] D. Cibotaru and S. Moroianu, *Odd Pfaffian forms*, Bulletin of the Brazilian Mathematical Society, New Series **52** (2021), 915–976.

[63] S. Moroianu, *Higher transgressions of the Pfaffian*, Revista Matemática Iberoamericana **38** (2022), 1425–1452.

[64] M. R. Douglas, *Holomorphic feedforward networks*, `arXiv:2105.03991`.

[65] A. Ashmore and F. Ruehle, *Moduli-dependent KK towers and the swampland distance conjecture on the quintic Calabi-Yau manifold*, Phys. Rev. D **103** (2021) 106028.

[66] V. Braun, T. Brelidze, M. R. Douglas and B. A. Ovrut, *Calabi-yau metrics for quotients and complete intersections*, JHEP **2008** (2008) 080.

[67] B. Shiffman and S. Zelditch, *Distribution of zeros of random and quantum chaotic sections of positive line bundles*, Communications in Mathematical Physics **200** (1999), 661–683.

[68] M. Cicoli, J. P. Conlon and F. Quevedo, *General analysis of large volume scenarios with string loop moduli stabilisation*, JHEP **10** (2008) 105.

Department of Physics and Astronomy, University of New Hampshire, Durham, NH 03824, USA
E-mail address: Per.Berglund@unh.edu

Department of Physics and Astronomy, University of New Hampshire, Durham, NH 03824, USA
E-mail address: Giorgi.Butbaia@unh.edu

Department of Physics and Astronomy, Howard University, Washington, DC 20059, USA
E-mail address: thubsch@howard.edu

Mandelstam Institute for Theoretical Physics, School of Physics, NITheCS, and CoE-MaSS, University of the Witwatersrand, Johannesburg, WITS 2050, South Africa
E-mail address: v.jejjala@wits.ac.za

Mandelstam Institute for Theoretical Physics, School of Physics, NITheCS, and CoE-MaSS, University of the Witwatersrand, Johannesburg, WITS 2050, South Africa
E-mail address: damian.mayorgapena@wits.ac.za

Department of Computer Science & Technology, University of Cambridge,
Cambridge CB3 0FD, UK
E-mail address: cm2099@cam.ac.uk

Department of Computer Science & Technology, University of Cambridge,
Cambridge CB3 0FD, UK
E-mail address: jt796@cam.ac.uk